AGU ADVANCING EARTH AND SPACE SCIENCES

JGR Solid Earth

RESEARCH ARTICLE

10.1029/2026JB034840

Stress Drop and Seismic Efficiency Distributions Over the Adriatic Indenter (European Southeastern Alps)

L. Cataldi[1], M. Picozzi[1], M. D'Amico[2], P. Morasca[3], D. Bindi[4], V. Poggi[1], G. Costa[5], A. Viganò[6], and D. Spallarossa[1,7]

[1]National Institute of Oceanography and Applied Geophysics – OGS, Udine, Italy, [2]Istituto Nazionale di Geofisica e di Vulcanologia (INGV) OE, Catania, Italy, [3]Istituto Nazionale di Geofisica e di Vulcanologia (INGV), Milan, Italy, [4]GFZ Helmholtz Centre for Geosciences, Potsdam, Germany, [5]MIGe, University of Trieste, Trieste, Italy, [6]Servizio Geologico, Provincia autonoma di Trento, Trento, Italy, [7]DISTAV, University of Genoa, Genoa, Italy

Key Points:

- Up-to-date, high-quality data set for the area of the European Southeastern Alps characterized by the presence of the Adriatic indenter
- Nonparametric Generalized Inversion Technique approach to compute the source parameters and investigate their spatial variability
- Insights on the mechanical behavior of faults in the study area and results available to calibrate regional relationships

Supporting Information:

Supporting Information may be found in the online version of this article.

Correspondence to:

L. Cataldi,
lcataldi@ogs.it

Citation:

Cataldi, L., Picozzi, M., D'Amico, M., Morasca, P., Bindi, D., Poggi, V., et al. (2026). Stress drop and seismic efficiency distributions over the Adriatic indenter (European Southeastern Alps). *Journal of Geophysical Research: Solid Earth*, *131*, e2026JB034840. https://doi.org/10.1029/2026JB034840

Received 19 MAY 2026
Accepted 21 JUN 2026

Author Contributions:

Conceptualization: L. Cataldi, M. Picozzi, D. Bindi, V. Poggi, D. Spallarossa
Data curation: L. Cataldi, D. Spallarossa
Formal analysis: M. Picozzi
Investigation: L. Cataldi, M. Picozzi
Methodology: L. Cataldi, M. Picozzi, M. D'Amico, P. Morasca, D. Spallarossa
Project administration: M. Picozzi
Resources: G. Costa, D. Spallarossa
Software: L. Cataldi, M. D'Amico, P. Morasca, D. Spallarossa
Supervision: M. Picozzi, D. Spallarossa
Validation: L. Cataldi, M. Picozzi, M. D'Amico, P. Morasca, D. Bindi, A. Viganò

Abstract

Seismic source parameters, such as seismic moment, stress drop, and radiated energy, are key to understanding earthquake dynamics and rupture processes. In this study, we apply a non-parametric Generalized Inversion Technique (GIT) to characterize the source properties of 735 earthquakes (local magnitudes $1.65 \le ML \le 4.55$) recorded between 2016 and 2024 in the area of the European Southeastern Alps characterized by the presence of the Adriatic indenter. The high-density seismic network coverage in the region allows for a robust, data-driven inversion of Fourier amplitude spectra to separate source, path, and site effects. Our results highlight significant spatial variations in seismic source parameters, revealing distinct mechanical properties of fault systems. We find a general increase in stress drop with depth and observe deviations from self-similar scaling, with apparent stress increasing with event size. The spatial distribution of the Savage-Wood efficiency suggests differences in dynamic fault strength, with high-efficiency events concentrated in the northeastern Italian Alps and Snežnik Mt. seismic area, respectively located in the Southeastern Alps Western sector and in the Dinarides seismotectonic domains, while lower-efficiency events are more common along the Tolmin-Idrija and Gemona-Tarcento fault systems and in the Schio-Vicenza-Lessini seismotectonic domain. These findings provide new constraints on the mechanical behavior of faults in the northeastern Adriatic indenter section and have implications for seismic hazard assessment and ground motion modeling. The study underscores the importance of accurate source parameter estimation in improving our understanding of regional seismotectonic and earthquake generation processes.

Plain Language Summary

In seismology, earthquake sources can be described using parameters related to the fault size, its rupture process, and the released energy. Studying the spatial distribution of these parameters allows us to identify the differences in the properties of the Earth's crust, such as rigidity and pore pressure. This is especially important in areas characterized by complex seismotectonic conditions. Here, we focus on a region with such characteristics, the Adriatic indenter, where the recent increase in the number of seismic monitoring stations has granted a large volume of high-quality data. We analyze 735 earthquakes that occurred in the area between 2016 and 2024 and estimate their source parameters by fitting the source spectra obtained from nonparametric inversion. We evaluate the spatial patterns in the distribution of the stress drop and seismic efficiency parameters, which are especially informative of the mechanics of faulting. We find that high-efficiency events are more concentrated in the northeastern Italian Alps and in the Snežnik Mt. area in Slovenia, while the Schio-Vicenza-Lessini seismotectonic domain is characterized by low seismic efficiency. We observe significant spatial variations revealing distinct mechanical properties of the fault systems that populate the region and suggesting the existence of differences in their dynamic strength.

1. Introduction

Seismic source parameters play a central role in advancing our understanding of earthquake dynamics and fault mechanics.

Their monitoring is essential for characterizing fault behavior and understanding the physical processes that govern fault slip and those leading to the generation of large earthquakes (e.g., Durand et al., 2020; Picozzi et al., 2019, 2022, 2023; Wang et al., 2019). These parameters, including seismic moment, stress drop, and seismic radiated energy, reveal critical information about the size, dynamics, and energy budget of seismic events. For example, seismic moment provides a measure of the total energy released during a rupture, while the corner

Visualization: L. Cataldi, A. Viganò
Writing – original draft: L. Cataldi, M. Picozzi
Writing – review & editing: L. Cataldi, M. Picozzi, M. D'Amico, P. Morasca, D. Bindi, V. Poggi, G. Costa, A. Viganò, D. Spallarossa

frequency reflects the rupture's spatial extent and temporal characteristics. Stress drop, which quantifies the decrease in shear stress on the fault during an earthquake, is a key parameter for understanding fault mechanics and rupture dynamics.

Accurate estimation of seismic source parameters is crucial not only for understanding the physics of past earthquakes but also for improving predictive models of ground shaking, which are fundamental for seismic hazard assessments and engineering design. Studies have increasingly emphasized the link between high-frequency ground shaking variability and source properties, such as stress drop, underscoring the importance of precise parameter estimation (e.g., Baltay et al., 2019; Bindi et al., 2019, 2023b; Oth et al., 2017).

Isolating the contribution of source properties from far-field seismic recordings remains a significant challenge. Reliable estimates of source parameters require assumptions about poorly constrained propagation effects, including near-surface site conditions. Propagation, site amplification, and source–path interactions can strongly distort the source signal (Abercrombie, 1995; Bindi et al., 2020; Hough, 1996; Shearer et al., 2019). Interpreting source spectra further depends on specific modeling frameworks, since many source parameters, such as stress drop, are not directly observable (Boatwright, 1980; Brune, 1970; Madariaga, 1976). As a result, the derived values are inherently influenced by assumptions regarding wave propagation (Bindi, Picozzi, et al., 2025; Chang et al., 2025; Shearer et al., 2024) and fitting procedures (Cochran et al., 2024). These model assumptions must be physically justifiable and explicitly accounted for when interpreting the results.

The accurate determination of source parameters was the focus of the recent community stress-drop validation initiative (Baltay et al., 2024). This benchmark study provided the occasion to compare results obtained using different approaches over the same data set by examining the consistency of stress-drop estimates for the Ridgecrest sequence in southern California. Results of this community initiative are reported in a special issue ("Improving Measurements of Earthquake Source Parameters," see Baltay et al., 2025). Therein, among many, Cochran et al. (2024) highlighted that spectral source parameter estimates can vary depending on spectral sampling, spectral model, and misfit criteria. Other studies have highlighted the importance of processing and modeling assumptions, as these can introduce biases that affect the final results (Bindi et al., 2023a, 2023b). The initiative also assessed how variations in modeling assumptions, treatment of propagation effects, and inversion strategies influence the inferred parameters and their scaling with earthquake size (Abercrombie et al., 2025). The scaling of source parameters with event size remains one of the most debated issues in earthquake source studies. The self-similarity hypothesis, first proposed by Aki (1967), predicts that stress drop remains constant, independent of magnitude. Support for this regime has been reported in large data sets spanning a range of tectonic environments (Shearer et al., 2006). However, analyses of individual seismic sequences frequently suggest systematic increases in stress drop with magnitude. Such behavior has been observed in central Italy for the 1997–1998 Colfiorito sequence (Malagnini et al., 2008), the 2009 L'Aquila sequence (Pacor et al., 2016), and the 2016–2017 Amatrice sequence (Kemna et al., 2021; Morasca et al., 2019). More recent work confirms similar trends in both the L'Aquila and Amatrice sequences (Morasca et al., 2022). Broader compilations of studies dedicated to assessing stress drop trends across different ranges of magnitude and different tectonic settings, using diverse methodologies, are provided in Cocco et al. (2016) and Baltay et al. (2024).

Over the decades, several methodologies have been developed to isolate the contribution of seismic source parameters from earthquake recordings, each method being characterized by strengths and limitations. Main approaches include:

1. Deconvolution Using Empirical Green's Functions (EGFs). With this technique, recordings from smaller, co-located earthquakes are used as proxies for path and site effects, allowing the isolation of the source contribution from larger events. It has been applied in both the time and frequency domains (e.g., Abercrombie, 2021; Mori & Frankel, 1990).
2. Coda Envelope Decay Modeling, which exploits the decay of seismic coda waves to infer source properties while minimizing the influence of path and site effects. It is particularly effective for regions with complex wave propagation (e.g., Mayeda et al., 2003; Shelly et al., 2021).
3. Generalized Inversion Technique (GIT), a robust method for jointly inverting Fourier amplitude spectra to separate source, path attenuation, and site amplification effects. GIT has been extensively used and refined since its introduction in the 1980s (e.g., among many Andrews, 1986; Bindi, Spallarossa, et al., 2025; Castro et al., 1990; Oth et al., 2011; Picozzi et al., 2017).

Each of these approaches addresses specific challenges in source parameter estimation, with their applicability largely determined by the quality and density of seismic data and the complexity of the tectonic setting.

The GIT, which we used in this work, is a technique that can be implemented using either parametric or non-parametric approaches, each suited to different data sets and objectives:

1. Parametric approach assumes a predefined functional form for attenuation with distance, which reduces the number of free parameters and simplifies the inversion process (e.g., Cataldi et al., 2023; Drouet et al., 2008; Zollo et al., 2014). While stable in cases of limited data coverage, the parametric approach is less effective in regions with complex geological settings.
2. Non-parametric approach, which is based on a data-driven strategy that avoids strong assumptions about functional forms, allowing for greater flexibility in modeling source, path, and site effects (e.g., Bindi et al., 2020; Oth et al., 2011; Wang et al., 2019). The non-parametric approach requires dense data coverage to ensure robustness but is well-suited to regions monitored by modern, high-density seismic networks.

The choice of GIT implementation—parametric or non-parametric—is influenced by data set characteristics and regional complexity. GIT has undergone continuous refinement, making it highly versatile and widely applicable. Recent developments in open-source software have further increased the accessibility and standardization of GIT. Furthermore, recent advances in dense seismic networks have further enhanced the precision and reliability of GIT, enabling detailed studies of small to moderate earthquakes. GIT thus became an indispensable tool for seismic source characterization, seismic hazard assessment, and earthquake engineering applications, and computational tools such as GITANES (Klin et al., 2018) and GITpy (D'Amico et al., 2024, 2025) have been developed to facilitate the implementation of both parametric and non-parametric approaches.

In this work, we apply the GITpy software to analyze data recorded in Northeastern Italy, which is a region characterized by a complex seismotectonic resulting from the interaction between the Eurasian and Adriatic microplates (the so-called Adriatic indenter; Bressan et al., 2003; Massironi et al., 2006; Reiter et al., 2018; Viganò et al., 2015). The area encompasses a variety of tectonic styles, including compressive faults, extensional structures and strike-slip systems, which collectively accommodate the ongoing deformation (e.g., Serpelloni et al., 2016). In the following, we adopt the same subdivision into main seismotectonic domains of interest for the study area as reported in Villani et al. (2024): BJO, Brenner-Jaufen Oetzal; CSA-MG, Central-Southern Alps and Meran-Giudicarie; DI, Dolomites Indenter; DIN, Dinarides; EOA, Engandine-Ortles Alps; ESEA, External Southeastern Alps; SEAE, Southeastern Alps (eastern sector), SEAW, Southeastern Alps (western sector); SVL, Schio-Vicenza-Lessini; TW, Tauern Window. This region has a history of moderate to strong seismicity and understanding its seismotectonic framework is critical for seismic hazard assessment and risk mitigation. Among many historical larger earthquakes that struck the North-Eastern Italy, we note the “1117 Verona Earthquake” (moment magnitude Mw 6.8) in the Venetian plain (Guidoboni et al., 2005), the “1046 Middle Adige Valley Earthquake” (Mw 6.0) along the Schio-Vicenza fault system (Guidoboni et al., 2019; Viganò et al., 2018), the “1695 Asolo Earthquake” (Mw 6.5) along the southernmost alpine fronts (Guidoboni et al., 2019), the “1511 Idrija Earthquake” (Mw ~6.8) linked to the Dinaric strike-slip fault system (Fitzko et al., 2005), and the more recent “1976 Friuli Earthquake” (Mw 6.5), a devastating event caused by thrust faulting along the southern Alps front, resulting in extensive damage and loss of life (Cipar, 1980; Slejko et al., 1999). An overview of the largest historical earthquakes for the region, as reported in the Italian Parametric Earthquake Catalogue (CPTI15; Rovida et al., 2020, 2022), is shown in Figure 1d.

In recent years, during the seismic monitoring performed by the Seismological Research Center of the National Institute of Oceanography and Applied Geophysics – OGS (Bragato et al., 2021; Sandron et al., 2023), we have observed a seismicity dominated by events of magnitude <4.5, often occurring along the southern Alps thrust front and secondary structures (Bressan et al., 2003; Pondrelli et al., 2006; Viganò et al., 2008). These smaller events provide valuable insights into fault behavior and stress redistribution in the region.

We focus our study on the seismicity recorded during the last decade, when the seismic networks in the area have reached a stable configuration and high density of stations.

So far, no comprehensive analysis of the source characteristics for the recorded seismicity at regional level has been made available yet. Previous studies on the same region (e.g., Castro et al., 1996 [CAS96]; Malagnini et al., 2002 [MAL02]; Franceschina et al., 2006 [FRA06]; Restivo et al., 2006 [RES06]; Klin et al., 2021 [KLI21];

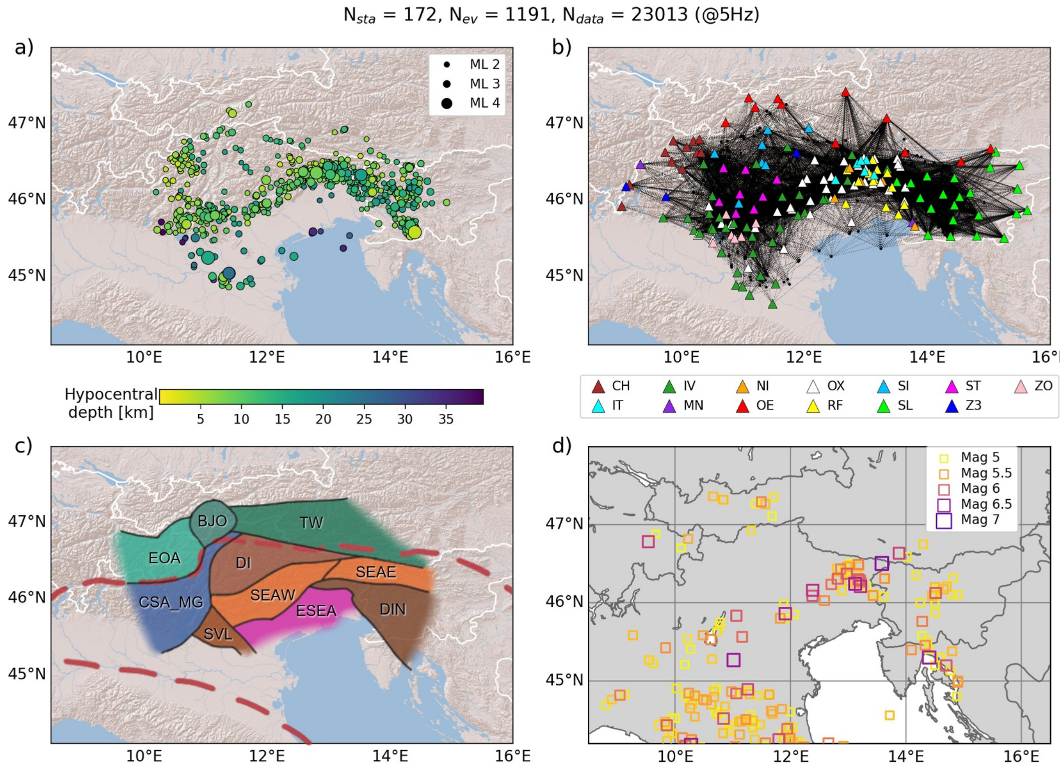

Figure 1. (a) Distribution of earthquakes colored per hypocentral depth. (b) Distribution of seismic stations colored per network code (see Table 1 for the list of networks). (c) The main seismotectonic domains of interest for the study area. They are, as reported in Villani et al. (2024): BJO, Brenner-Jaufen Oetzal; CSA-MG, Central-Southern Alps and Meran-Giudicarie; DI, Dolomites Indenter; DIN, Dinarides; EOA, Engandine-Ortles Alps; ESEA, External Southeastern Alps; SEAE, Southeastern Alps (eastern sector), SEAW Southeastern Alps (western sector); SVL, Schio-Vicenza-Lessini; TW, Tauern Window. The approximate position of the Adriatic indenter, as reported in Massironi et al. (2006), is represented as dashed red line. (d) Historical seismicity for the area for all events with magnitude above 5 in the time range 1000–2020, taken from the Italian Parametric Earthquake Catalogue (CPTI15; Rovida et al., 2020, 2022).

Cataldi et al., 2023 [CAT23]) focused on data sets reduced with respect to the one considered here both in terms of number of events and of stations.

We present the seismic source characterization results for 735 seismic events (in the local magnitude range 1.65 < ML < 4.55) recorded by 172 stations in the time period 2016–2024, with over 20,000 spectral amplitude values associated with each frequency in the range 1.2–25 Hz (Figures 1a and 1b).

By extending the data set to the whole European Southeastern Alps area characterized by the presence of the Adriatic indenter, our aim is to study the spatial distribution of source parameters to highlight the possible existence of fault segmentation and heterogeneities.

2. Data Set

The initial pool of events included 13,568 earthquakes available from the OGS bulletin (https://www.crs.inogs.it/bollettino_new/; see Open Research section) for the time period 2016–2024, selecting all available records within an epicentral distance of 120 km, sampled at 100 Hz.

This work represents the first attempt in this zone to jointly use all accelerometric and velocimetric data available from the seismic networks monitoring the area, both permanent and temporary. This allows to considerably expand the data set with respect to the aforementioned studies focused on the same region (e.g., CAS96, MAL02, FRA06, CAT23), both in terms of number of events and of stations; the list of used stations is available in the data repository (see Open Research and References sections).

10.1029/2026JB034840

Accurate preliminary data selection and processing were performed on this preliminary set of events. In particular, the pre-processing consists of:

1. Instrumental correction and automated picks using the procedure proposed by Scafidi et al. (2019).
2. Event re-location using the *NonLinLoc* software (Lomax et al., 2000).
3. Local magnitude ML computation by averaging the station magnitude estimates and considering the zero-magnitude attenuation model calibrated by Di Bona (2016) for Italy, but without applying station corrections, to have homogeneous estimates of the magnitude size for all events.

For locating the earthquakes, we used the same 1D regional velocity model (Riggio & Russi, 1984) as in the OGS localizations, which allows us to interpret the inversion results in the light of the well-constrained focal depth parameters. The resulting depth values are comparable with those reported by the OGS and Istituto Nazionale di Geofisica e Vulcanologia (INGV) bulletins. Uncertainties in event locations are mostly within 2 km horizontally (Erh) and 3 km vertically (Erz) (Figure S1 in Supporting Information S1).

For each selected recording, the vectorial composition of the Fourier amplitude spectrum (FAS) of the two horizontal components is computed for 98 frequency values between 0.05 and 47 Hz on the S-wave time window, and smoothed using the Konno and Ohmachi (1998) algorithm ($b = 40$). The time window itself is selected based on the fraction of cumulated energy (i.e., 90% for data recorded within an hypocentral distance of 25 km; 80% for distances between 25 and 50 km and 70% for larger distances; cf. Pacor et al., 2016), with a minimum duration of 4 s and a maximum duration of 20 s. As it emerges from the aforementioned studies, this is a consolidated strategy that allows to obtain high quality data. The reason for choosing a variable length based on cumulative energy is the need to ensure a sufficiently long time window for the larger events, to avoid the bias effects observed in Bindi et al. (2023b). The applied variable length criterion also takes into account the hypocentral distance, in order to strike a balance between ensuring a sufficiently long time window for larger events and avoiding the inclusion of surface waves at larger hypocentral distances for smaller events.

A subset of data has then been extracted from the preliminary data set based on the following quality criteria:

1. Events localized using at least 12 seismic phases (P and S picks);
2. Events with ML $\geq$ 1.0;
3. Events with Erh $\leq$ 3 km and Erz $\leq$ 5 km;
4. Events with azimuthal gap less than 200°;
5. Fourier spectra having at least 60% of points that satisfy the condition SNR (signal-to-noise ratio) $\geq$ 2.5 (equal for all frequencies)
6. Events recorded by a minimum of 8 stations and stations having at least 8 records

The final selected data set consists of 1191 seismic events recorded by 172 stations belonging to different networks (Figure 1), with as many as 22,130 available spectral amplitudes at the most sampled frequencies. The number of available spectral amplitudes varies with the frequency, due to the chosen constraint on SNR and to the variable window lengths. Even so, the good data coverage allows to select the wide frequency range of 0.1–47 Hz for the subsequent analyses, as the corresponding number of available spectral amplitudes is 6607 and 7114 respectively. All frequencies in the range 1.3–25 Hz have more than 20,000 associated available amplitudes.

The main characteristics of the selected data set are summarized in Figure 2, in terms of distribution of the number of records with respect to focal depth, hypocentral distance and ML. Most data comes from shallow events (hypocentral depth shallower than 20 km) with low magnitude (ML between 1 and 3). The selected data set provides an excellent spatial coverage up to 120 km, as evidenced by the magnitude-distance distribution (Figure 2d) and by the ray path map (Figure 1b). Moreover, the data set is characterized by good quality scores in terms of Erh, Erz, azimuthal gap and number of phases used in each localization (cf. Figure S1 in Supporting Information S1).

3. Method

In a first step, we adopt the non-parametric, data-driven GIT for extracting empirical functions describing the source, the site response and the attenuation from FAS (Castro et al., 1990). Then, in a second step, we invert the empirical source spectra and the empirical attenuation curves to estimate the source parameters (i.e., corner

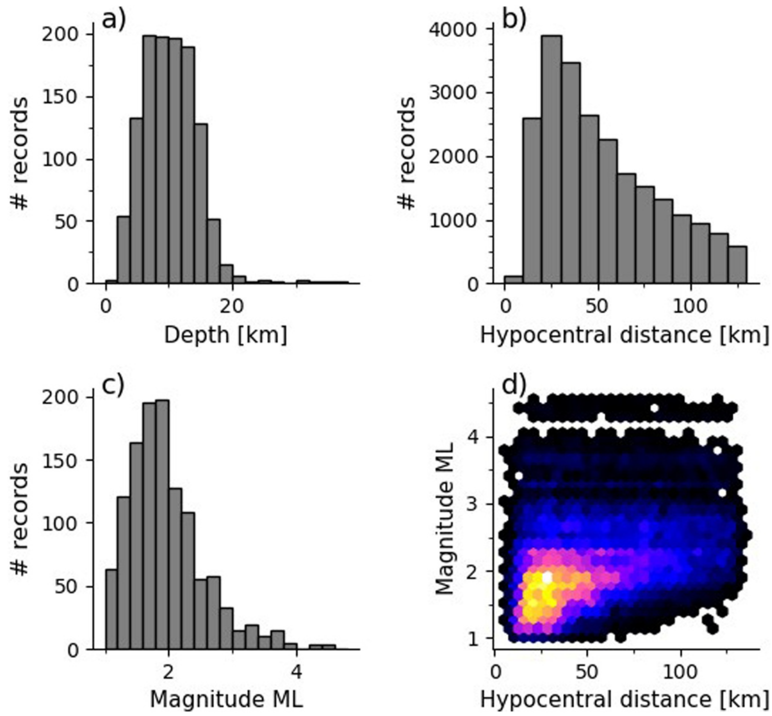

Figure 2. Histograms showing the distribution of data with respect to: (a) hypocentral depth, (b) hypocentral distance, and (c) magnitude. (d) Density plot of the data distribution with respect to hypocentral distance and magnitude.

frequency (f_c), seismic moment (M_0), radiated energy of the Brune source model (E_S), Brune, 1970), and the parameters describing the crustal attenuation (i.e., geometrical spreading (n) and quality factor (Q)).

In the GIT analysis the main assumption is that the S-wave FAS, U, can be modeled in log domain as linear combination of acceleration source spectra, S, spectral attenuation with distance, A, and site response Z:

$$\log_{10} U_{ij}\,(f, r_{ij}) = \log_{10} S_i(f) + \log_{10} A(f, r_{ij}) + \log_{10} Z_j(f), \tag{1}$$

where i and j indicate the ith earthquake and the jth station, respectively, f the frequency and r_{ij} the hypocentral distance.

The inversion is performed on the acceleration FAS using the software GITpy (D'Amico et al., 2024, 2025), which is derived by the GIT implementation proposed by Oth et al. (2011), employs a non-parametric one-step scheme and is designed with an object-oriented structure, allowing for community contributions and continuous refinement. For each frequency, the inversion has been performed in a least-square sense (Paige & Saunders, 1982). Based on the data set characteristics, the hypocentral distance range from 5 to 120 km has been discretized into 60 bins, each 2 km wide.

Non-parametric GIT does not make a priori assumptions on the functional form of the attenuation, site and source operators; regardless, two unresolved degrees of freedom affecting Equation 1 must be removed by adding some constraints. Following a consolidated strategy in GIT studies, we adopted the following: (a) for all frequencies, the attenuation operator is set to 1 at a reference hypocentral distance, here set to $r_0 = 10$ km; (b) to eliminate the linear dependence between the source and site terms, the average site amplification of a set of selected reference stations is constrained using a numerical amplification model. The value of r_0 was chosen based on the distribution of the hypocentral distances in the data set (Figure 2b), as the data points at hypocentral distances lower than 10 km are sparse. Furthermore, we require that the attenuation smoothly varies with distance. We refer to the original work of Castro et al. (1990) for details on the implementation of these constraints.

Concerning the reference station selection, most of the considered stations lack near-surface shear-wave velocity profiles and consequently also a standard classification based on international standards adopted in building code

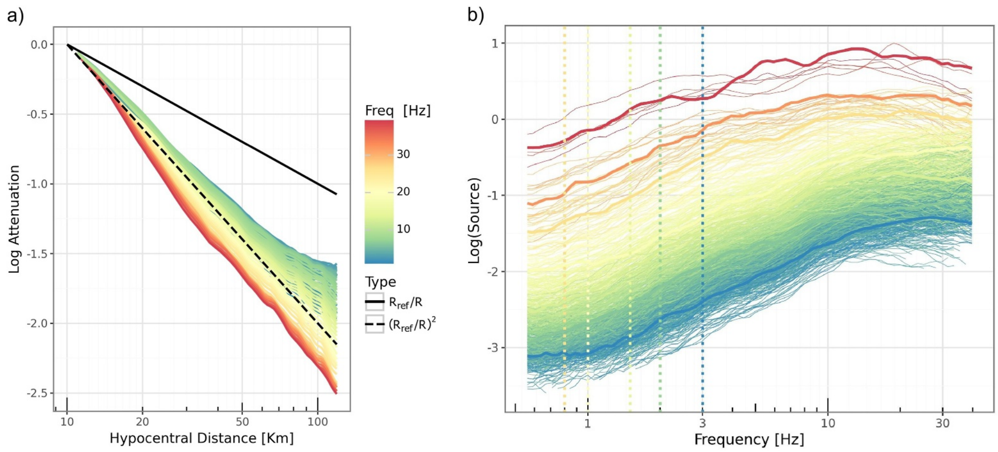

Figure 3. (a) Attenuation-distance curves obtained from the nonparametric inversion (colored lines); the geometrical spreading, $1/R$, and the $1/R^2$ trend are also plotted (black continuous and dot-dashed lines, respectively). (b) Empirical acceleration source spectra (colored per ML). The spectra of a few events with different magnitudes are highlighted in bold. The frequency thresholds subsequently used for spectral fitting (cf. Table 2) are shown as vertical dotted lines, with color corresponding to the minimum magnitude for which they are applied.

provisions (e.g., Eurocode 8; CEN, 2006). For some networks an alternative classification is available through dedicated studies (e.g., KLI21 for OX, Cultrera et al., 2022 for IV and MN), helping in the definition of a reference site amplification. We have performed tests with different sets of candidate stations with spectral characteristics compatible with those of a reference site following the previous studies in the area (RES06, KLI21) and eventually settled on the methodology proposed by Bindi and Kotha (2020). The resulting set of 12 reference stations (IV.PTCC, MN.TUE, NI.PURA, OE.MYKA, OE.SOKA, OX.BAD, OX.CIMO, OX.CSM, OX.FUSE, OX.MLN, OX.PRED, ST.PANI) has an almost flat amplification with amplitudes within a factor 2 from their ensemble average. The selected stations belonging to the OX network are among those identified as having neutral or deamplifying site response in KLI21. The remaining stations are categorized as either EC-8 A or EC-8B soil class in the Engineering Strong Motion Database (Luzi et al., 2020). All reference stations were also checked for possible vertical amplifications by running a preliminary GIT inversion on the vertical component, finding none, and compared with earthquake H/V curves available from the STATION service (Tarchini et al., 2024; Figure S2 in Supporting Information S1).

Regarding the numerical amplification model used to constrain the average amplification of the reference stations, a high-frequency kappa (κ) decay (Andreson & Hough, 1984) was imposed, with a value of $\kappa = 0.02\ s$. This value was chosen to produce source spectra that, on average, are consistent with the Brune model (see also the consistency checks performed on a subset of events with ML $\geq$ 2.5, reported in Figure S3 of Supporting Information S1).

4. Results for Nonparametric GIT Inversion: Path and Site Functions

The non-parametric GIT procedure splits the FAS into source, propagation and site terms which are not yet described in terms of a seismological model. Source spectra and site amplifications are represented by generic vectors, while the propagation term is described by a matrix which contains the variability of the spectral amplitudes with frequency and hypocentral distance. Before analyzing the results of the non-parametric inversion, the goodness of fit of the non-parametric curves was checked by computing the residual distributions (see Figure S4 in Supporting Information S1). The residuals, computed as the difference between observed and predicted spectral values, do not show any trend with frequency, and they have mean close to zero with standard deviations of about 0.2.

The resulting non-parametric attenuation functions obtained at different frequencies as a function of distance are reported in Figure 3a. They are characterized by an evident dependency on frequency and show an overall monotonical decrease with distance at a rate that increases with frequency. We performed a residual analysis to verify the possible presence of biases introduced by the use of a path correction independent of source depth in our

Table 1
List of Used Seismic Networks and Number of Associated Stations Used in This Study

Code	# Of used stations	Network description
CH	11	Switzerland Seismological Network, operated by Eidgendssisch Technische Hochschule - Swiss Seismological Service (ETH)
IT	6	Italian Strong Motion Network, operated by Presidency of Counsil of Ministers - Civil Protection Department (PCM - DPC), Italy
IV	37	Italian National Seismic Network, operated by Istituto Nazionale di Geofisica e Vulcanologia (INGV)
MN	2	Mediterranean Very Broadband Seismographic Network, operated by ING
NI	5	North-East Italy Broadband Network, operated by Istituto Nazionale di Oceanografia e di Geofisica Sperimentale (OGS) and University of Trieste (UniTS)
OE	11	Austrian Seismic Network, operated by Zentralanstalt für Meterologie und Geodynamik (ZAMG)
OX	39	North-East Italy Seismic Network, operated by OGS
RF	14	Friuli Venezia Giulia Accelerometric Network, operated by UniTS
SI	7	Province Südtirol network, operated by ZAMG
SL	22	Seismic Network of the Republic of Slovenia, operated by Slovenian Environment Agency (ARSO)
ST	8	Trentino Seismic Network, operated by Geological Survey-Provincia Autonoma di Trento
Z3	4	AlpArray, operated by ETH
ZO	6	Dynamic Planet (PD) multiparametric Northern Italy seismic network, operated by INGV

non-parametric attenuation functions. We thus analysed the distribution of the attenuation values obtained by correcting each observed FAS for the matching site and source non-parametric GIT functions, against the corresponding non-parametric GIT attenuation curve, at a set of selected frequencies. Even with the obvious limitation of high-depth events only being recorded at higher hypocentral distances, no bias whatsoever as a function of hypocentral depth emerges from the residual distributions (cf. Figure S5 in Supporting Information S1).

Overall, the non-parametric GIT attenuation functions tend to align along the $1/r^2$ trend, and distinctly far from the commonly assumed $1/r$ trend, reflecting the underlying behavior of the geometrical spreading (cf. Figure S6 and Text S1 in Supporting Information S1 for a description of the spectral attenuation curves based on a standard parametric model of geometrical spreading and anelastic attenuation). The same trend was observed in other studies both in Italy and in other regions (e.g., among many, Cantore et al., 2011 in Irpinia; Pacor et al., 2016 in central Italy). As discussed in Yenier and Atkinson (2015) and in Pacor et al. (2016), the geometrical spreading at close distances is often assumed to follow a $1/r$ trend based on homogeneous whole space approximation. However, since real propagation media are far from homogeneous, it is common to observe faster spreading at short and intermediate distances, and numerical simulations in typical layered earth models have also confirmed that the distance decay in the epicentral area can be described by geometrical spreading with exponent greater than 1 (Chapman & Godbee, 2012; Frankel, 1991). In our case, using a tri-linear geometrical spreading model (Text S1 and Figure S6 in Supporting Information S1), we obtained an exponent of $n_1 = 1.77$ for distances R < 40 km.

Figure 3b shows the resulting non-parametric source spectra (colored per magnitude). It can be observed how the spectral shape changes depending on the magnitude, which particularly affects the lowest frequency for which the SNR condition is met. To take into account this effect, the frequency bandwidth used in the subsequent fitting (Table 2) is selected magnitude-wise based on visual inspection of the source spectra in the displacement domain, as shown in the Supporting Information (Figure S7 in Supporting Information S1).

Regarding the site response functions obtained from the non-parametric GIT inversion, we show a representative subset of results in Figure 4. A complete visualization of all site functions is available in the Supporting Information (Figure S8 in Supporting Information S1). The authors direct readers to studies specifically focused on site effect estimation in the region (RES06, KLI21) for a detailed description and analysis of individual cases, which lies beyond the scope of this study.

Table 2
Frequency Range Limits Used to Perform the Apparent Source Fitting for Different Magnitude Ranges

ML range	f_{min} [Hz]	f_{max} [Hz]
1.5–2.0	3.0	40.0
2.0–2.5	2.0	40.0
2.5–3.0	1.5	40.0
3.0–3.5	1.0	40.0
≥3.5	0.8	40.0

Our site response results are in very good agreement, within uncertainty, with independent estimates from the literature (Figure 4), especially those of KLI21, who applied a GIT inversion specifically designed to estimate site effects in the same area. The comparison shows that our site response function agrees well with KLI21 in terms of fundamental frequency, although our results tend to yield lower amplification values. This effect can be attributed to differences in the reference amplification conditions. To assess the impact of the assumed reference condition, the GIT curves can be scaled by the average reference site amplification (cf. Figure S9 in Supporting Information S1). In some cases (AGOR, MTLO) the results are consistent in terms of both the amplification level and the fundamental frequency. The same holds true for the vertical amplification curves (dashed lines in Figure 4). For a limited set of stations (e.g., GORI, PURA, STOL in Figure 4) not included in the KLI21 data set, the results are verified against the parametric inversion curves of CAT23, finding a good agreement within the associated uncertainties.

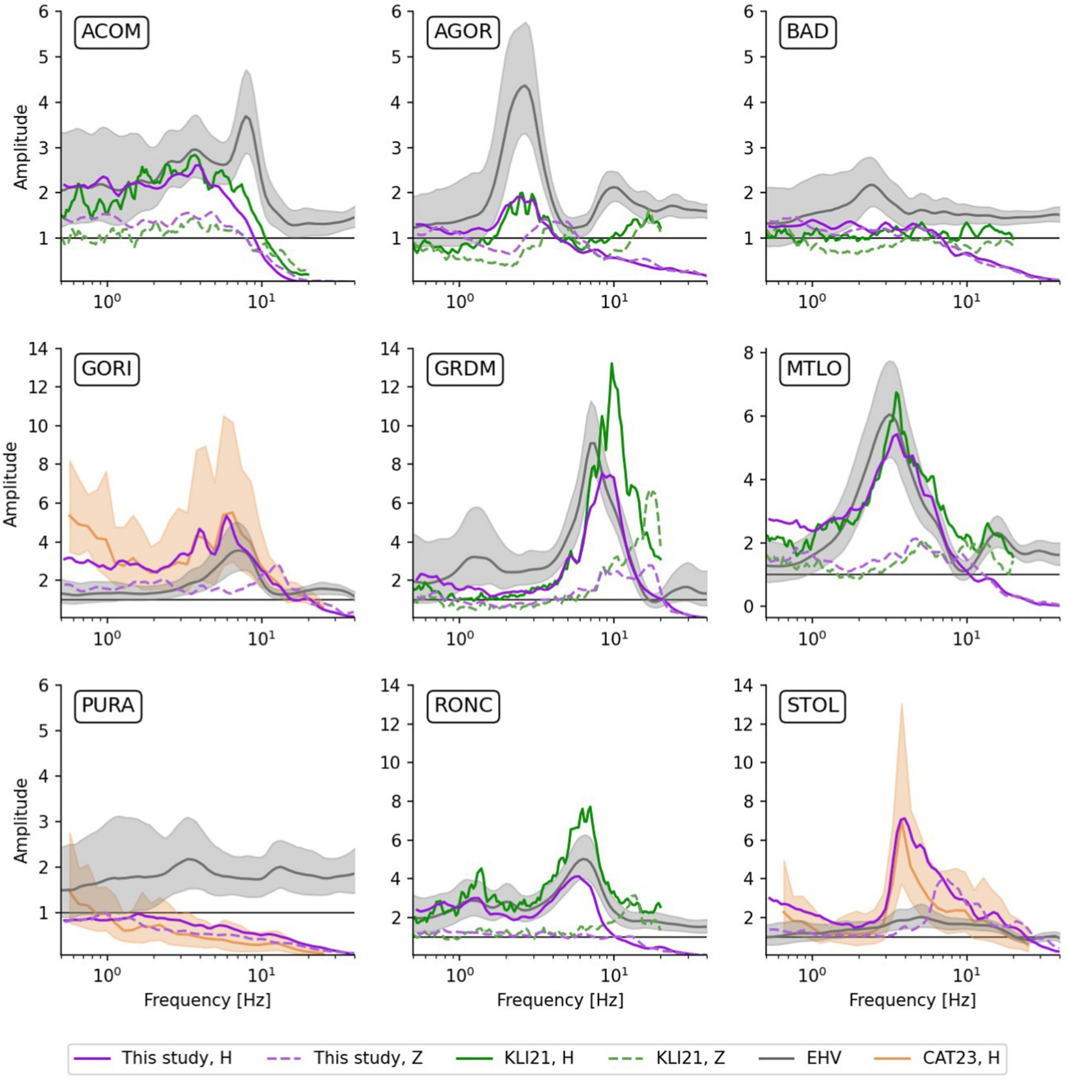

Figure 4. Example of nonparametric site response functions, both horizontal (solid lines) and vertical (dashed lines). The earthquake H/V curves from STATION service (EHV) are reported in gray for comparison. Where available, the corresponding curves reported in KLI21 and CAT23 are also shown for comparison. The shaded areas represent the standard error, where available.

For completeness, the GIT site functions are also compared with the earthquake H/V ratios (EHV) available from the STATION service (Tarchini et al., 2024), showing that the two estimates are on average in good agreement. This finding is consistent with previous observations (e.g., Parolai et al., 2004). A more detailed analysis of the GIT site functions, however, is beyond the scope of this paper.

Overall, considering the good agreement with the available KLI21 curves, the site functions derived from GIT are also suitable for being used in stochastic simulations, such as generating synthetic seismograms at a given station. However, as discussed before, it is important to note that all GIT results, especially site transfer functions, are inherently influenced by the a priori assumptions made on the reference sites. In this study, using a set of stations selected on the basis of the regional average (with site functions provided in the data repository; cf. Availability Statement and References sections) helps to mitigate the bias that would arise from relying on a single, poorly constrained station.

5. Source Parameter Estimates From GIT-Derived Source Spectra

Here, we focus on a posteriori fitting of the source functions to obtain seismic parameter estimates. A brief overview of the fitting of the non-parametric attenuation functions is also provided in the Supporting Information.

The source spectra terms $S(f)$ are fitted to the omega-square source model (Brune, 1970) to estimate the seismic moment M_0 and the corner frequency f_c:

$$S(f) = \Omega_0 \frac{(2\pi f)^2}{1 + \left(\frac{f}{f_c}\right)^2} \tag{2}$$

$$\Omega_0 = \frac{R_{\vartheta\varphi} FV}{4\pi\rho\beta^3 r_0} M_0 \tag{3}$$

where $R_{\vartheta\varphi} = 0.55$ is the average radiation pattern for S waves (Boore & Boatwright, 1984), $F = 2$ is the free-surface amplification factor, and $V = 1$ is the energy partition factor, set to unitary as the inversion is performed on the vectorial composition of the two horizontal components. We use the same reference distance $r_0 = 10\ km$ as in the attenuation inversion. To correctly catch the possible dependency of the results on the focal depth, instead of using a single average value of S-wave velocity (β) and soil density (ρ) for all the earthquakes, we associate the β and ρ estimates extracted from a simplified 1-D version of the Magrin and Rossi (2020; hereby, MR20) model to each source. The used velocity model is available in the data repository (see Availability Statement and References sections).

The GIT decomposition yields a source spectrum for each event that fits all recordings at different stations in a least-squares sense. Consistent with previous studies (e.g., Bindi et al., 2020; Morasca et al., 2022; Pacor et al., 2016), the non-parametric GIT source spectra reproduce the median of the apparent source spectra, obtained by correcting each recording for site amplification and spectral attenuation as determined by GIT. Due to the good azimuthal coverage and the requirement of at least eight stations per event, potential directivity effects are assumed to average out (Pacor et al., 2016), thereby enabling robust estimates of corner frequency and seismic moment.

The constraint used for the reference site condition (i.e., $\kappa = 0.02\ s$) was selected in such a way that, on average, the source shows a flat acceleration spectrum (Oth & Kaiser, 2014; Pacor et al., 2016). To check for possible deviations from a flat acceleration spectrum at high frequencies for each event, we evaluate the slope (referred to as source-kappa) of the non-parametric source spectra in scale semi-log above 10 Hz. This is similar to Andreson and Hough's (1984) approach for kappa, but applied to the non-parametric GIT source spectra. The resulting values of the source-kappa are normally distributed with mean $\kappa_S = 0.000 \pm 0.007\ s$, confirming that on average the source spectra are not affected by the high-frequency decay effect. Individual spectra might still show limited effects at high frequencies, such as in the case of smaller earthquakes with corner frequencies near the upper considered frequency range, or large events with source spectral shape deviating from the omega-square one.

We determine the corner frequency and seismic moment for each event by fitting the Brune model (Equation 2) to the non-parametric source spectra, converted to displacement. The only constraints applied to the fit are that M_0 be positive and f_c be in the 0–100 Hz range, to avoid any dependency of the results on a limitation of the solution space. As mentioned in Section 4, different frequency bandwidths are adopted for different magnitude ranges, chosen through visual inspection of the inverted non-parametric source curves to ensure a high signal-to-noise ratio over the relevant frequency range. To anchor the seismic moments to a reference seismic catalog, we follow the procedure of Bindi, Spallarossa, et al. (2025), using the INGV moment magnitudes (ISIDe Working Group, 2007; https://terremoti.ingv.it/). The average difference between the inverted moments and the catalog values, calculated over a subset of events with Mw > 3.2, is applied as a systematic correction by shifting all source spectra accordingly.

The full list of source parameters for the 735 events for which the fit converged is available in the data repository (see Availability Statement and References sections). The data set is composed of shallow events with local magnitude ranging between ML 1.65 and ML 4.55; corresponding seismic moments range between 2.1×10^{11} Nm and 2.7×10^{15} Nm and corner frequencies between 0.57 Hz and 28.27 Hz. The range for seismic moments is compatible with the observations reported in FRA06 and related to regional events with ML < 5 not exceeding 2×10^{15} Nm.

The agreement between the non-parametric source spectra and the fitted omega-squared model is shown in Figure 5 for a selection of events spanning the considered magnitude range; the frequency band used for each fit is also shown. The residuals between model-derived and non-parametric spectral amplitudes (cf. Figure S10 in Supporting Information S1) show good overall consistency, with the mean residual remaining close to zero across the entire frequency range and dispersion increasing only above 20 Hz.

Given the obtained estimates for seismic moment and corner frequency, the Brune stress drop $\Delta\sigma$ is computed assuming a circular rupture of radius r with uniform stress drop (Borok, 1959; Eshelby, 1957; Madariaga, 1976, 1979) as:

$$\Delta\sigma = \frac{7}{16}\frac{M_0}{r^3}, \tag{4}$$

$$r = \frac{k\beta}{f_c}, \tag{5}$$

where $k = 0.37$ (Brune, 1970, 1971) and, as described above, the shear wave velocity values β are referred at hypocentral depth. The estimated stress drop values for all events are reported in the data repository (see Open Research and References sections), together with the associated variability, which is calculated using error propagation on the standard errors for M_0 and f_c. $\Delta\sigma$ values range between 0.02 and 9.13 MPa, with a median value of 0.44 MPa and an average value of 0.72 MPa which matches the estimate provided in FRA06 (0.73 MPa). The average error calculated with error propagation is 0.07 MPa. Seismic moments are plotted against corner frequencies in Figure 6, together with theoretical lines of constant Brune stress drop.

Previous studies focused on northeast Italy tend to confirm the source self-similarity regime hypothesis for the region (FRA06, CAT23). Following Kanamori and Rivera (2004), we perform a linear fit between the logarithm of source parameter estimates and compare it to the following parametrization:

$$M_0 \propto f_c^{-(3+\varepsilon)}, \tag{6}$$

in which the ε parameter measures the deviation from stress drop self-similarity ($\varepsilon = 0$ in the case of self-similarity, $\varepsilon < 0$ and $\varepsilon > 0$ if the stress drop respectively increases or decreases with event size).

An orthogonal linear regression between $\log(M_0)$ and $\log(f_c)$ is performed for the entire data set ($\varepsilon = -0.63 \pm 0.14$ with 95% confidence interval), as well as for events with hypocentral depths between 5 and 10 km ($\varepsilon = -0.35 \pm 0.21$), between 10 and 15 km ($\varepsilon = -0.35 \pm 0.22$), and for events with depths above 15 km ($\varepsilon = -0.18 \pm 0.35$). Considering the uncertainty associated with the parameter ε, the null hypothesis of self-similar scaling can be rejected at 95% confidence level for all but the data subset corresponding to deeper events. This result suggests an apparent breaking of self-similarity, with inverse proportionality between stress

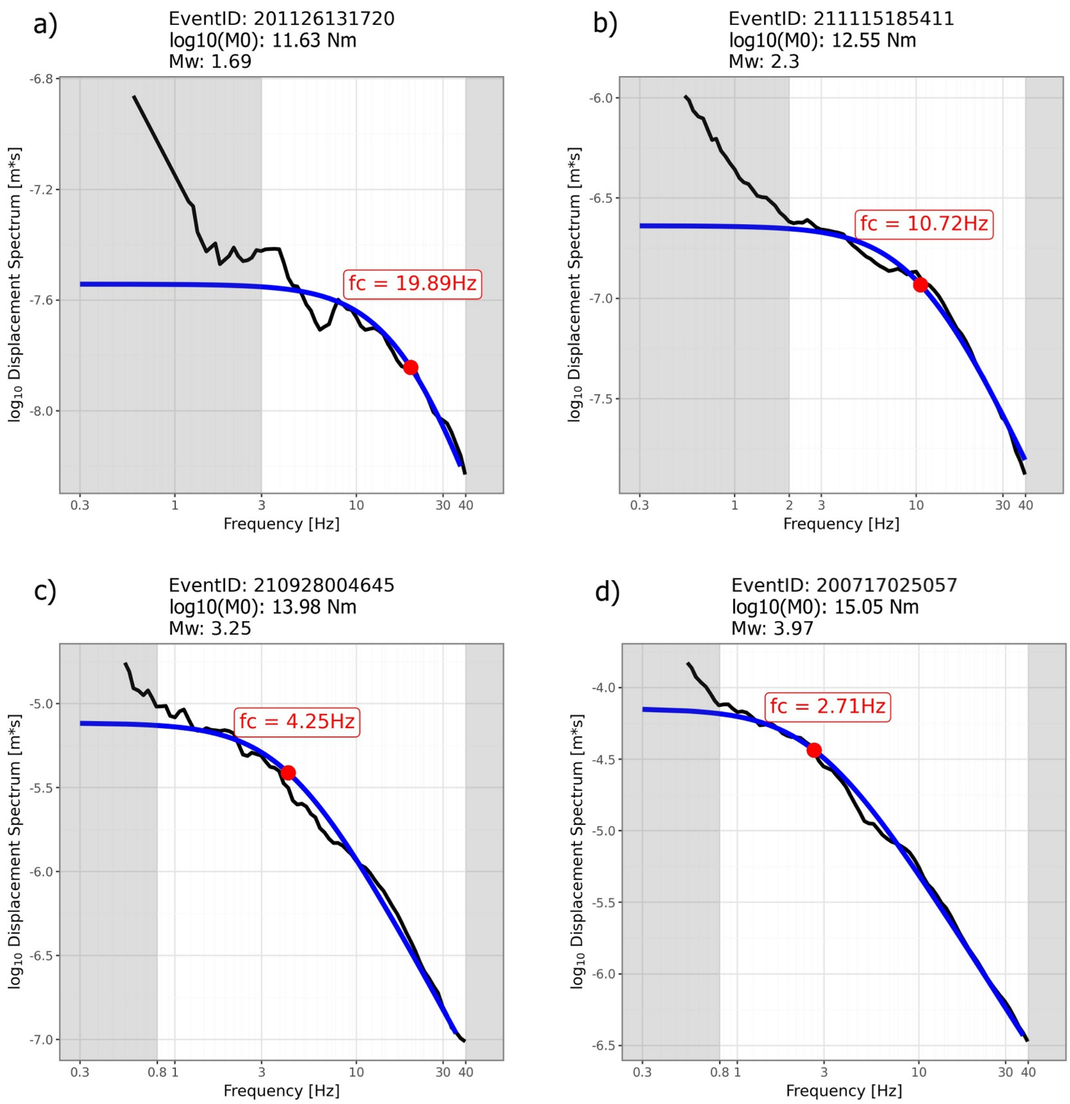

Figure 5. Example of nonparametric source spectra (black lines) and corresponding fitted spectra (blue lines). The fit is performed over the frequency range depicted in white, while the gray bands represent the unused frequency bands for each fit.

drop and earthquake size, for the whole data set, and for smaller, shallower events in particular. When the calculated stress drop values are directly compared to seismic moment values (Figure 7) instead of using the epsilon proxy, a clear increase in their value with increasing event size is evident despite the large scatter. The regression presented in Figure 7 was produced through a robust linear fit on the binned data set; a piecewise fit would also be possible, as done for example, in Pacor et al. (2016), but it would not produce a meaningful difference in the minimization of information loss by the two models (as indicated by the modified Akaike score, cf. Figure S11 in Supporting Information S1). The larger variability of $\Delta\sigma$ for smaller events can be interpreted as an effect of the higher sensitivity of small ruptures to stress and strength heterogeneities in the focal volume (Calderoni et al., 2019). As the stress drop estimates are computed using the stratified MR20 velocity model, and thus it is considered the best estimates for S-wave velocity and rock density at each hypocentral depth, we expect them to be more informative than the epsilon proxy, which instead assumes common, average values for those soil properties. A stress drop scaling effect is also consistent with studies focusing on different areas of the world and relying on diverse methodologies, which observed larger events such as mainshocks to have higher average stress drop than smaller events, although favoring a piecewise interpretation rather than a linear one (Baltay et al., 2019; Boyd et al., 2017). However, the trend noted here should not be extrapolated outside the magnitude range of the

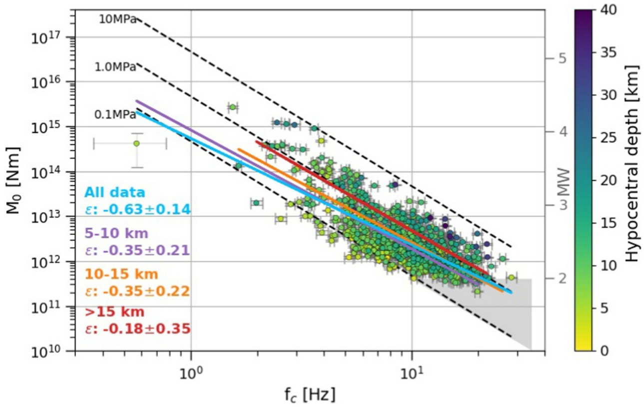

Figure 6. Seismic moment M_0 and corner frequency f_c, colored per hypocentral depth (dots), and 95% probability confidence limits for the estimated parameters (horizontal and vertical gray lines, respectively). M_0 and f_c scaling relation for the whole data set (blue line), for events with hypocentral depth between 5 and 10 km (purple line), for the range 10–15 km (orange line) and for depth larger than 15 km (red line). Dashed black lines are theoretical lines of constant Brune stress drop. Gray triangle represents the area where possibly missing events would locate.

underlying data set without further study, as this could lead to unrealistic predicted values for larger and smaller earthquakes (Abercrombie & Baltay, 2025). In fact, the observational limit of the data set depends on the combination of magnitude and frequency bandwidths; possibly missing microseismic events would populate the area represented in gray in Figure 6. Some studies (Chen et al., 2025; Zhang et al., 2022) found that using a depth-dependent attenuation correction could reduce the magnitude-dependence of stress drop. These observations must thus be interpreted keeping in mind that the stress drop values could be somehow overestimated due to the possible tradeoff between the source and the attenuation components, whose simplified model does not catch the increase in Q values with depth, as argued by Abercrombie et al. (2021).

The source parameter results we obtained can be compared to the CAT23 study which focused on roughly the same area; visual representations of the results regarding the f_c, M_0 and $\Delta\sigma$ parameters are available in the Supporting Information (Figures S12 and S13 in Supporting Information S1). It should be noted, however, that a direct comparison is possible only for six events which are common to the two data sets. For those events, we find the estimates (reported in Table 3) in good agreement, in particular those of seismic moments. We find a systematic bias of 0.36 units of Mw on average between the corresponding moment magnitude estimates, which is a reasonable consequence of the different constraint assumptions and especially of the anchoring of our values to a reference seismic catalogue. When considering the full data sets, we notice that CAT23 found a higher average stress drop and did not identify any magnitude scaling. This apparent disagreement with respect to our results can be explained by the different composition of the data sets, which in CAT23 was much smaller and included mostly higher magnitude events (74% of the CAT23 events have $M \geq 3$).

Along with corner frequency and seismic moment, we also estimate the total radiated seismic energy (E_S) and its uncertainty obtained from source inversion following Ide and Beroza (2001). E_S is computed as the integral of the non-parametric source spectra, with asymptotical extrapolation to an omega-square model at low and high frequencies, to mitigate bandwidth effects that could otherwise underestimate the total energy, particularly for lower magnitudes. Figure 8 shows E_S versus M_0 values, together with the relationship between their logarithmic values obtained through linear regression (i.e., $\log(E_S) = -8.738 + 1.266 \log(M_0)$). The resulting trend agrees with the value proposed in FRA06 for the same region ($\log(E_S) = -9.06 + 1.30 \log(M_0)$). Interestingly, the energy-to-moment scaling appears to be consistent across different studies regarding low-intermediate magnitude crustal events: Bindi et al. (2020) report 1.31 for small events in Central Italy, whereas Picozzi et al. (2022) observe a similar range of slope values not only for events in Central Italy, but also in southern California and Japan. A visual comparison is provided in the (Figure S14 of Supporting Information S1).

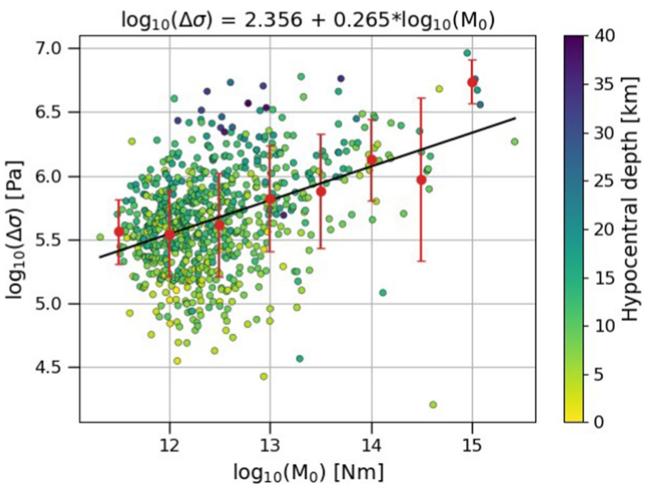

Figure 7. Stress drop, $\Delta\sigma$, versus seismic moment, M_0, with values colored per hypocentral depth, median (red dots), and standard deviation (red lines) of $\Delta\sigma$ computed for bins of M_0, and best fitting model (black line).

In turn, E_S can be used to compute the apparent stress τ_a as:

$$\tau_a = \frac{\rho\beta^2 E_S}{M_0} \tag{7}$$

where $\rho\beta^2$ is the crustal shear modulus calculated with the values extrapolated from the MR20 model. The apparent stress is proportional to the ratio between total radiated seismic energy and the seismic moment, and it corresponds to the radiated energy per unit area per unit slip. Consequently, low values of τ_a correspond to events with lower rupture velocity and longer duration. A systematic increase in apparent stress with moment magnitude is reported in many studies (e.g., Abercrombie, 1995; Kanamori et al., 1993; Mayeda & Walter, 1996; Perez-Campos & Beroza, 2001), and would suggest a difference in the source properties of small and large earthquakes. The same

Table 3
Comparison Between Source Parameters Obtained in This Study and Those Reported in Cataldi et al. (2023) for a Subset of Events

	f_c	M_0 [Nm]	MW	f_c	M_0 [Nm]	MW	f_c	M_0 [Nm]	MW
	ID 160719223649			ID 160810023805			ID 161222084353		
CAT23	9.86	$1.78E+13$	2.76	5.49	$4.79E+13$	3.05	8.69	$1.45E+13$	2.71
This study	10.7	$3.89E+12$	2.32	4.72	$2.24E+13$	2.83	8.60	$4.93E+12$	2.39
	ID 170209081408			ID 170323131107			ID 170324174708		
CAT23	6.6	$2.69E+14$	3.56	11.35	$3.98E+13$	3.00	9.63	$1.66E+13$	2.74
This study	5.13	$1.07E+14$	3.28	9.02	$1.04E+13$	2.61	8.94	$3.04E+12$	2.25

trend is also found in our results obtained for the northeast Italy data set, where an increase of the radiated energy with seismic moment corresponds to an increase in the apparent stress by roughly one order of magnitude (black dashed lines in Figure 8). However, there is no consensus on this trend, and many other seismological observations instead found no dependency of source processes from event size. As Beeler et al. (2003) pointed out, most seismic source models themselves do not theorize an increase in apparent stress with moment; this is also the case of the Brune source model, in which the apparent stress for S waves is a fixed fraction of the static stress drop.

Before proceeding to discuss our results, it should be noted that all the source parameter estimates we presented directly depend on the Brune omega-square assumption, which is most commonly applied and allows our estimates to be more directly comparable to those of other studies. This dependency passes through the corner frequency estimates, as they are subsequently used for the calculation of other source parameters that directly ($\Delta\sigma$) or indirectly (E_S, τ_a, η_{sw}) depend on f_c. There is a known tradeoff between f_c and the high frequency fall-off, or spectral decay. To address this issue, one could try to simultaneously fit the corner frequency and the slope n of the spectral model, instead of fixing $n = 2$ like in the Brune assumption. This was done for example, by Neely et al. (2025), finding that the use of a different spectral decay model modified the observed f_c and $\Delta\sigma$ distributions in the results. However, as Trugman and Shearer (2017) stated clearly, this further fitting does not solve the inherent tradeoff between the stress drop scaling and the spectral decay, which occurs because «the high-frequency falloff rate substantially affects the results only well above the corner frequency, a portion of the spectra, that is, observable only for the larger events». In fact, models with $n = 2$ and stress drop scaling and models with $n < 2$ and stress drop self-similarity may have a risible difference in misfit, equally explaining the high frequency content of larger events (see e.g., Figure 9 in Trugman & Shearer, 2017). There is also the underlying issue of the available bandwidth, as the uncertainties in the resolution of the spectral decay are expected to trade-off with the ratio of f_c to the maximum usable frequency of the spectrum. We acknowledge that our results are depending on these underlying, inherent tradeoffs. In the following section, we follow the energy balance approach suggested by Beeler et al. (2003) to interpret our results and discuss a physically based explanation of the seemingly increase of apparent stress with seismic moment.

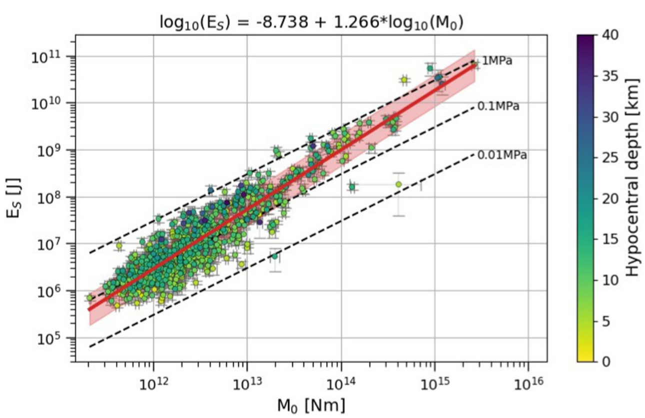

Figure 8. Radiated energy, E_s, versus seismic moment, M_0, with data colored per hypocentral depth, and 95% probability confidence limits for the estimated parameters (horizontal and vertical gray lines, respectively). The best fitting model and its associated ±1 standard deviation is shown in red. Dashed black lines are theoretical lines of constant apparent stress, τ_a.

6. Discussion: Energy Balance and Seismic Efficiency

When a fault slips, only a limited portion of the total strain energy accumulated during the inter-seismic period is released as seismic waves, while the remaining is dissipated through other processes like heat or the creation of new fractures. Seismic efficiency thus provides insights into the mechanics of faulting.

Faults characterized by rupture processes with higher seismic efficiency can release a significant portion of the accumulated strain energy as seismic waves, leading to stronger ground shaking and potentially destructive earthquakes. Conversely, faults showing rupture processes with low seismic efficiency result in less seismic radiation during earthquakes, being more energy consumed as off-fault damage or frictional heating.

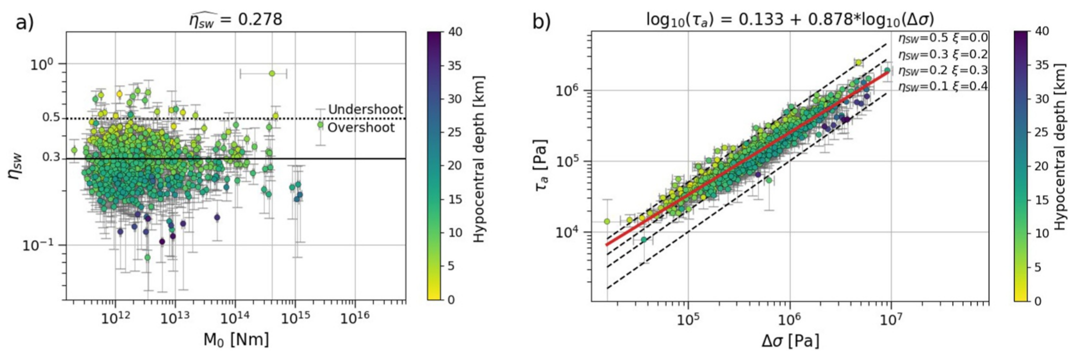

Figure 9. (a) Savage-Wood efficiency, η_{sw}, versus seismic moment, M_0, with data colored per hypocentral depth and 95% probability confidence limits (vertical gray lines); the zero overshoot condition ($\xi = 0, \eta_{sw} = 0.5$, black dashed line) and the threshold proposed by Beeler et al. (2003) ($\xi = 0.2, \eta_{sw} = 0.3$, solid black line) are reported for comparison. (b) Apparent stress, τ_a, versus stress drop, $\Delta\sigma$, with data colored per hypocentral depth, and 95% probability confidence limits for the estimated parameters (horizontal and vertical gray lines, respectively), best fitting model (red line). Dashed black lines are theoretical lines of constant efficiency, η_{sw}, and overshoot, ξ.

Understanding these variations helps in assessing the seismic hazard associated with different faults. However, since the total energy released cannot be determined by seismological data, it is common practice referring to the Savage-Wood ratio, η_{sw} (Savage & Wood, 1971).

The parameter η_{sw} is determined as the ratio of apparent stress to the static stress drop:

$$\eta_{SW} = \frac{\tau_a}{\Delta\sigma}. \tag{8}$$

The Savage-Wood ratio can be compared to the overshoot ξ, which measures whether the static stress drop is smaller ($\xi < 0$, undershoot) or larger ($\xi > 0$, overshoot) than the dynamic stress drop (Beeler et al., 2003):

$$\eta_{SW} = 0.5 - \xi, \tag{9}$$

As Beeler et al. (2003) pointed out, although most dynamic crack models assume a positive overshoot (e.g., Madariaga, 1976), negative overshoot can be induced in the case of dynamic slip termination due to local fault healing. The overshoot also measures the dynamic strength relative to the stress level, which can thus be inferred by analyzing the Savage-Wood efficiency.

Figure 9a shows η_{SW} calculated for the 735 earthquakes analyzed in this study versus seismic moment. It is worth noting that special care was put into obtaining reliable estimates of η_{SW}, by dealing with the attenuation and bandwidth limitations that can consistently affect the error on apparent stress. Indeed, as previously mentioned, the Ide and Beroza (2001) methodology for seismic energy calculation was applied, and all terms contributing to η_{SW} are obtained by considering the depth-dependent soil properties (density and S-wave velocities, taken from the MR20 tomographic model). These precautions allow to interpret the resulting η_{SW} estimates as an indirect indicator of dynamic fault strength.

Constant overshoot is represented in Figure 9a by straight lines with zero slope. The η_{SW} values do not show systematic dependency on seismic moment and have a median value of 0.278, which is consistent with the values reported in laboratory measurements (e.g., $\widehat{\eta_{SW}} = 0.22$ in Lockner & Okubo, 1983; cf. Beeler et al., 2003 and references therein). More specifically, Beeler et al. (2003) proposed the criterion $\eta_{SW} > 0.3$ to infer evidence of dynamic weakening exceeding that seen in laboratory experiments of stick-slip faulting and in observations of stress drop for small, induced earthquakes. The results obtained for our data set are mostly consistent with the lab η_{SW} values, which were obtained in dry conditions. However, we highlight a subset of events with shallower focal depth showing higher Savage-Wood ratio values, and in some cases even meeting the undershoot condition ($\eta_{SW} > 0.5$). Undershoot is generally related to a condition of increased dynamic weakening, which might be caused by shear melting or by pore fluid pressurization with self-healing rupture (Beeler et al., 2003). In our case, being rather low the magnitude of the earthquakes showing undershoot (i.e., between Mw ~1.7 and ~3.6), we

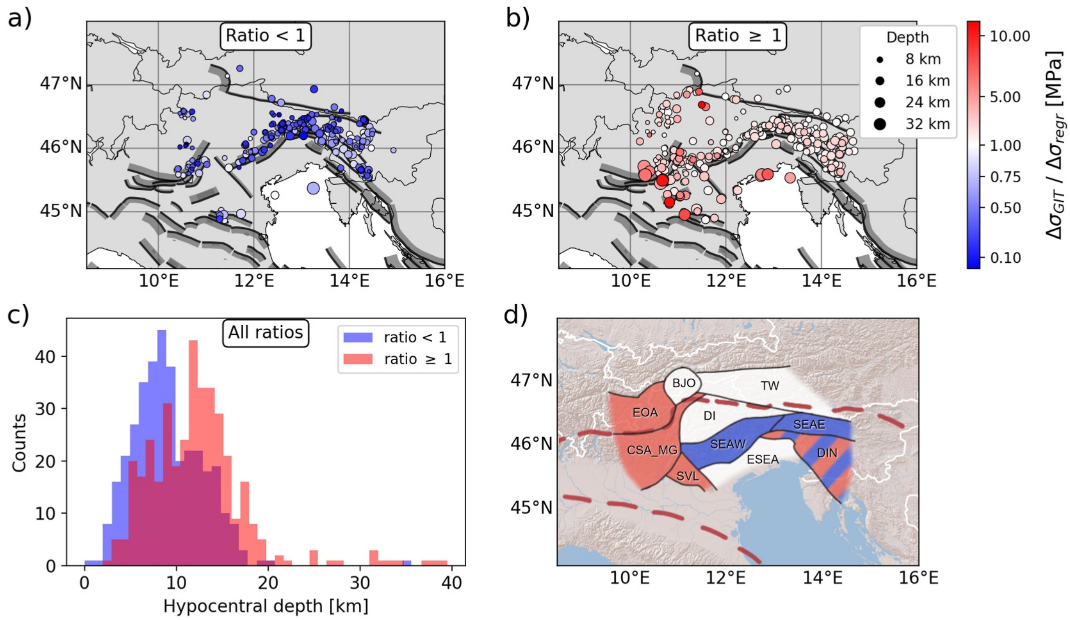

Figure 10. Geographical distribution of the stress drop ratio (dots), calculated as the ratio between values obtained from the GIT parameters ($\Delta\sigma_{\text{GIT}}$) and the corresponding theoretical values calculated using the best fitting model ($\Delta\sigma_{\text{regr}}$). For better clarity the results are divided between values below one (blue, Panel a) and above one (red, Panel b). The corresponding distributions in terms of hypocentral depth are reported in Panel (c). A simplified classification of the seismotectonic domains based on the predominant stress drop ratio condition is proposed in Panel (d). Domains for which no cluster of events with equal stress drop ratio existed are colored in white, domains hosting clusters of events with high or low stress drop ratio are colored in red and blue respectively. Domains hosting both clusters of high and low stress drop ratio events are represented as red and blue striped areas. The approximate position of the Adriatic indenter, as reported in Massironi et al. (2006), is represented as dashed red line.

hypothesize the rupture processes with high η_{SW} being associated with high pore pressure. The increase in pore pressure by water accumulation in karst systems in Northeastern Italy was discussed by Bragato (2021), even in relation to its potential in triggering significant seismic events in the region.

To better understand the η_{SW} results, we take a step back and we analyze the heterogeneity observed in its components and in the stress drop especially (additional plots of the distribution of stress drop and apparent stress are reported in Figures S15 and S16 in Supporting Information S1, respectively). We previously noted a trend of stress drop increasing with magnitude, as observed in Figure 7, and acknowledged the inherent tradeoffs and possible uncertainties. However, Figure 7 not only displays a large scatter in the stress drop distribution, it also hints at a dependency of the distribution on hypocentral depth. Such a behavior would be in line with observations available in literature (e.g., Baltay et al., 2019; Bindi et al., 2023b; Boyd et al., 2017) of an increase of stress drop with earthquake depth. We thus investigate the relative stress drop to highlight both the variation with depth and the spatial variation, which can hint for different faults properties. The relative stress drop displayed in Figure 10 is calculated as the ratio between the stress drop obtained from fitted GIT parameters ($\Delta\sigma_{\text{GIT}}$, colored points in Figure 7) and the corresponding theoretical value calculated for the same seismic moment value using the best fitting model obtained from the distribution itself ($\Delta\sigma_{\text{regr}}$, black line in Figure 7). Figures 10a and 10b respectively display the events for which the stress drop value is lower than the theoretical value (ratio <1, 52% of the events) and equal or higher than the theoretical value (ratio >1, 48% of the events). The respective distributions in terms of hypocentral depth values (Figure 10c) are in agreement with the observation made on Figure 7 and confirm that events with $\Delta\sigma$ values below the best fit model have on average shallower hypocentral depths than events with $\Delta\sigma$ values above the best fit model. A similar observation is reported in Goertz-Allmann and Edwards (2014) for small to medium earthquakes in Switzerland. As for the geographical distribution of the stress drop ratios, we observe a lower spatial scatter for events with ratios below one, which remain more grouped along the main thrust systems and in the EOA subregion. At the same time, events with stress drop ratios above one are more spatially dispersed, with the events with higher ratios and hypocentral depths located both in the southern areas of the

Veneto plains (ESEA), in the Giudicarie region (CSA_MG) and near the Apennine front (SVL). A simplified classification of the seismotectonic domains based on the predominant stress drop ratio condition (i.e., condition displayed by at least 50% of the events in the domain, with a minimum of 20 events) is proposed in Figure 10d. We make an exception for the classification of the DIN domain, to highlight its peculiarity of hosting almost the same percentage of positive and negative stress drop ratio events (53% (109 events) and 47% (96 events) respectively).

As discussed by Bindi, Spallarossa, et al. (2025) for central and southern Italy, a large lateral variability may make it difficult to isolate stress drop trends with depth when considering large areas with complex tectonics. Ignoring site-dependent spectral decay can also result in significant variation in corner frequency estimates among stations with apparent good fits, as observed by Chang et al. (2025) in the case of single-spectrum fitting. Therefore, we acknowledge that the observed increase in stress drop with depth could potentially be influenced by the adopted spectral attenuation model, particularly by its lack of explicit dependence on earthquake hypocentral depth. However, it is also important to emphasize that there is no consensus in the literature on whether incorporating a depth-dependent Q model would fully explain or significantly reduce the observed trend of increasing stress drop with depth. This uncertainty arises because the attenuation effect is integrated over the entire path, with the most significant Q reductions typically occurring near the surface. As a result, accounting for depth-dependent attenuation may not fully compensate for the observed depth-dependent stress drop patterns, or even generate more complex trends as shown recently by Bindi, Picozzi, et al. (2025). To support these stress drop pattern findings, we produce a comparison with a few well recorded events analyzed through spectral ratio. We followed a simplified procedure using an approach similar to the one of the EGFs deconvolution (cf. Introduction), analyzing the spectral ratios of the GIT-derived source spectra. A brief overview of the analysis is provided in the Supporting Information (Text S2 in Supporting Information S1), and the results are reported in Figure S17 and Table S1 of Supporting Information S1. The results of this test show different shapes of the spectral ratios for events in the SEAW/SEAE domains with respect to events in the CSA-MG and SVL domains, supporting our observation that the stress drop regime appears to be different in the considered domains. As shown in Figure S17 of Supporting Information S1, the empirical spectral ratios can also be compared to the theoretical ratios reconstructed from GIT-derived parameters. Mismatches can be interpreted as either an underestimation of the corner frequency of small events, or as a result of the depletion of the high-frequency spectral level in some larger events in the low stress drop area, where the spectral shapes deviate from the omega-square model. A further development would be to fit the spectral ratios independently in order to estimate the corner frequency and seismic moment values for each pair of events. However, such an analysis is beyond the scope of this work and would require more systematic research to investigate whether the omega-square source assumption could lead to the complexities in the larger events' spectral shapes being wrongly interpreted as underestimation of the corner frequencies of smaller events.

A similar line of reasoning to that applied to stress drop analysis can be followed in investigating the heterogeneities in the seismic efficiency. Again, we take a step back and analyze the τ_a versus $\Delta\sigma$ trend (Figure 9b). In that plot, lines of constant overshoot (i.e., constant η_{sw}) are represented as black dashed lines with unitary slope. The robust fit of data shows a slope lower than one, indicating that, while the apparent stress increases with $\Delta\sigma$, still the Savage-Wood efficiency decreases, corresponding to an increment in relative dynamic strength. This suggests that the larger events in the data set have a deficit in radiated energy, as they actually display low efficiency and high overshoot. This trend is not unprecedented, and it was extensively observed and analyzed by Beeler et al. (2003) on the Californian Cajon Pass data by Abercrombie (1995).

Figure 9a also hints at a dependency of η_{sw} on source depth (see also Figure S18 in Supporting Information S1), suggesting that apparent stress and stress drop have a different variation with depth. It is worth keeping in mind that the chosen attenuation modeling might impact on our estimates. As previously discussed, the lack of full correction for depth-dependent Q attenuation could possibly produce an artificial increase in stress drop with depth. This is partially mitigated using intrinsic frequency dependent whole-path attenuation (Goertz-Allmann & Edwards, 2014), as done in this study. To investigate the possible depth dependency, we look at our data in terms of relative efficiency, which is calculated as the difference between η_{sw} values and their median value (i.e., $\Delta\eta_{sw} = \eta_{sw} - \widehat{\eta_{sw}}$, Figure 11). This allows us to identify two distinct subsets according to the hypocentral depth: shallower events are associated to the highest positive $\Delta\eta_{sw}$ deviations (i.e., relative undershoot condition, which corresponds to higher dynamic stress drop, Beeler et al., 2003), while deeper events prevalently show negative $\Delta\eta_{sw}$ (i.e., relative overshoot condition, which corresponds to lower dynamic stress drop, and larger amount of energy spent as heat or the creation of new fractures).

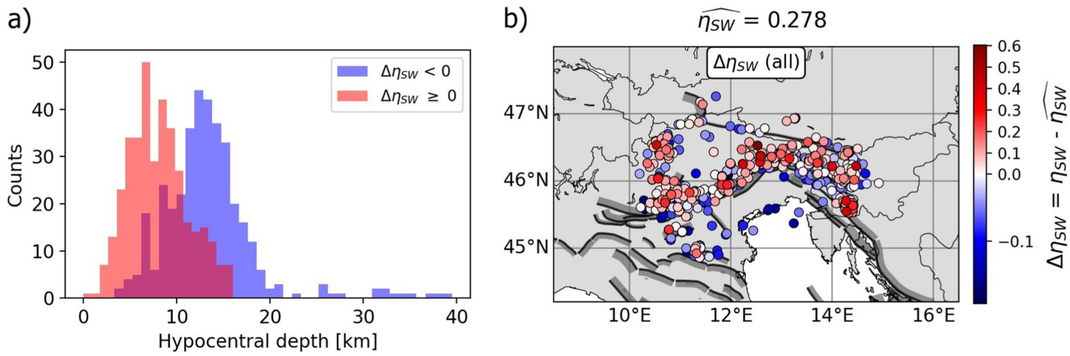

Figure 11. (a) Histograms showing the distribution of positive (red) and negative (blue) relative efficiency values, $\Delta\eta_{sw}$, with respect to hypocentral depth. (b) Geographical distribution of all the considered events (dots), with data colored per relative efficiency.

Since, at a first glance, Figure 11 suggests an uneven spatial distribution of $\Delta\eta_{sw}$, we investigate the spatial distribution of η_{sw} itself, which could help to identify areas displaying characteristic efficiency behavior. We define three categories based on the efficiency values reported in Beeler et al. (2003): events with very low efficiency ($\eta_{sw} < 0.2$, 10% of total events), events with efficiency in the range that is typical for laboratory and small induced earthquakes ($0.2 \leq \eta_{sw} \leq 0.3$, 53% of total events), and events with high efficiency ($\eta_{sw} > 0.3$, 37% of total events). We notice that almost half of the considered events fall in the typical efficiency range, while the remaining half mostly displays higher efficiency. Only 10% of the events display very low efficiency levels, which are also associated with higher magnitudes and higher hypocentral depths. Some interesting features can be evidenced in the spatial distribution of η_{sw}. Their corresponding macro areas are highlighted in Figure 12 and identified with labels that follow the division of the region into the seismotectonic domains identified in Villani

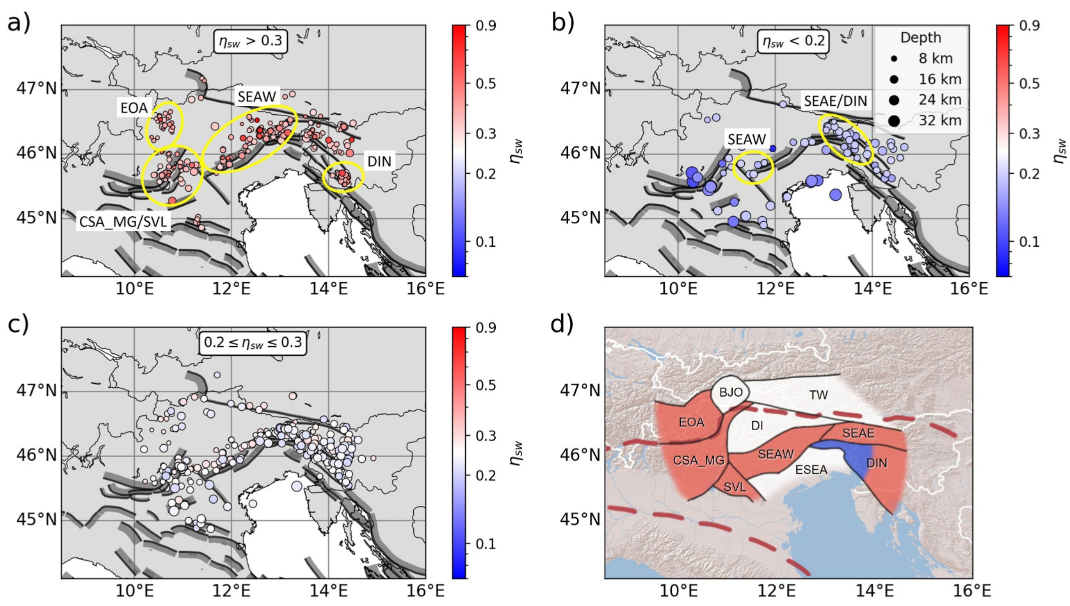

Figure 12. Geographical distribution of the resulting Savage-Wood efficiency (dots), divided between values above (red, Panel a) and below (blue, Panel b) the [0.2, 0.3] range defined as typical for laboratory and small induced earthquake observations by Beeler et al. (2003). Peculiar areas, for which clusters of positive and negative efficiency values are observed, are highlighted in yellow. Events with typical efficiency values are reported in Panel (c). A simplified classification of the seismotectonic domains based on the predominant efficiency condition is proposed in Panel (d). Domains for which no cluster of events with equal efficiency range existed are colored in white, domains hosting clusters of events with high efficiency are colored in red. The domain DIN hosts both clusters of high and low efficiency events, represented as red and blue areas respectively. The approximate position of the Adriatic indenter, as reported in Massironi et al. (2006), is represented as dashed red line.

10.1029/2026JB034840

et al. (2024). A simplified classification of these domains based on the predominant efficiency condition (either above 0.3 or below 0.2, with a minimum of 10 events) is also proposed in Figure 12d; again, an exception is made for DIN, to highlight its peculiarity of hosting the highest number of low efficiency events (23) among all domains, despite having a majority of high efficiency events (54). These peculiar areas show the following features:

- Areas indicated as EOA, CSA_MG/SVL (related to the Zebrù and South Giudicarie local fault systems, respectively) and DIN (especially the southern part in the Snežnik Mt. area in Slovenia, characterized by the Raša and Idrija faults) are markedly populated by earthquakes with high efficiency.
- Overall, the whole northeastern Italian Alps arc (section SEAW and part of SEAE) appears characterized by an abundance of events with relatively high efficiency.
- The western limit of the northeastern Alps arc (the portion of the SEAW area at the border with CSA_MG/SVL and ESEA), between the north-east to south-west trending Valsugana thrust system and the north-west to south-east trending Schio-Vicenza fault (DISS, 2021), is characterized by events with low efficiency.
- On the eastern side of the investigated area, we observe the presence of events characterized by both low and high efficiency (i.e., areas SEAE/DIN and DIN in Figure 12b, respectively). Notably, the low-efficiency cluster observed in SEAE/DIN corresponds to the faults system responsible for some of the larger historical earthquakes (i.e., the 1511 Idrija and 1976 Friuli Earthquakes).

Overall, the distribution of η_{sw} as well as of the stress drop appears to be spatially heterogeneous, suggesting the presence of crustal volumes and faults with peculiar mechanical characteristics. High-efficiency event clusters are most observed in the SEAW, EOA and DIN seismotectonic domains, while low-efficiency events are present in the SEAW and DIN seismotectonic domains.

7. Conclusions

In this study, we performed a comprehensive seismic source characterization of the northeastern section of the Adriatic indenter, mostly covering Northeastern Italy, using the non-parametric Generalized Inversion Technique (GIT). By analyzing a data set of 1191 seismic events recorded between 2016 and 2024, we extracted key source parameters for 735 of these events, including seismic moment, corner frequency, stress drop, and radiated energy. Our findings provide new insights into the spatial variability of seismic source properties and their implications for regional seismotectonic processes. As discussed, source parameter studies such as ours must face an inverse problem and the non-uniqueness of its solution. In simpler terms, alternative solutions cannot be distinguished based on goodness-of-fit criteria alone, and uncertainties such as the tradeoff between stress drop increase and spectral decay remain. Further analyses with different methodological approaches would provide a useful comparison for the results, although experiences such as the community stress-drop validation initiative teach us that such comparison might not be straightforward. In our analysis, we do not impose assumptions on stress drop dependence with magnitude or depth; instead, we make reasonable assumptions about reference site conditions and how attenuation varies with distance. Thus, accepting that we must rely on reasonable choices, we obtained source spectra exhibiting specific characteristics and we interpreted the results in the light of those assumptions. The general consistency of our source parameters with previous studies makes us confident that we avoided overinterpretation. The expanded data set analyzed with respect to previous studies allowed for a more detailed regional analysis of results.

Our results confirm the complexity of the seismicity in the region, characterized by variations in stress drop, seismic efficiency, and apparent stress across different fault systems and depth ranges. Specifically, we observed:

- A spatially heterogeneous distribution of both stress drop ratio and Savage-Wood efficiency, suggesting distinct mechanical behaviors among fault systems. Notably, high-efficiency events cluster in areas such as the northeastern Alps arc and the Snežnik Mt. area seismic zones (located inside the SEAW and DIN seismotectonic domains respectively), while low-efficiency events are prevalent along the Thiene-Cornuda and Schio-Vicenza fault systems (at the border between SEAW and SVL seismotectonic domains) and in the western portion of the DIN domain.
- Apparent deviations from self-similar scaling, with an increase in apparent stress with event size, which might indicate differences in rupture dynamics across different fault structures.

These findings contribute to a more refined understanding of the seismic hazard in the European Southeastern Alps area characterized by the presence of the Adriatic indenter, with practical implications for ground motion prediction models and seismic hazard assessments, particularly in a region with a history of moderate to strong seismicity. The key areas of fault segmentation and mechanical heterogeneity identified in this work will be the object of further, targeted analyses focusing on the spatiotemporal evolution of dynamic strength during earthquakes on local preexisting faults (e.g., as done by Calderoni et al., 2019; Picozzi et al., 2021, 2023). Additional efforts will be made to improve the attenuation modeling to further constrain source parameters.

By providing a robust data set and methodological framework, this work lays the foundation for further research into the physical mechanisms governing earthquake generation in Northeastern Italy and beyond. Moreover, the obtained source parameters will be used to calibrate attenuation laws for the area under study to rapidly estimate seismic moment and radiation energy during seismic monitoring routine operations as done for central Italy by the Ramones service (Spallarossa et al., 2021).

Conflict of Interest

The authors declare no conflicts of interest relevant to this study.

Availability Statement

Figures and maps were made with Matplotlib version 3.8.4 (Hunter, 2007; The Matplotlib Development Team, 2024), available under the Matplotlib license at https://matplotlib.org/. The GITpy software (version 1.0.3) was used to perform GIT inversion and subsequent source spectra fitting. It is licensed under the GNU Lesser General Public License (LGPL) v3.0 and is available at (D'Amico et al., 2024). The results of this study (including apparent source spectra, site and attenuation functions, and all the resulting fitted source parameters) are available at (Cataldi et al., 2025). The facilities of the European Integrated Data Archive (EIDA; Strollo et al., 2021), the National Institute of Oceanography and Applied Geophysics – OGS, and the Italian Civil Protection Department archives were used in the creation of this manuscript, for accessing data and metadata with International Federation of Digital Seismograph Networks (FDSN) network identifiers CH (Swiss Seismological Service At ETH Zurich, 1983), IT (Presidency of Counsil of Ministers - Civil Protection Department, 1972), IV (INGV, 2005), MN (MedNet Project Partner Institutions, 1990), NI (OGS & University of Trieste, 2002), OE (ZAMG, 1987), OX (OGS, 2016), RF (University of Trieste, 1993), SI (ZAMG, 2006), SL (Slovenian Environment Agency, 1990), ST (Geological Survey-Provincia Autonoma di Trento, 1981), Z3 (AlpArray Seismic Network, 2015), and ZO (Massa et al., 2021). The FAS curves calculated from the data retrieved from the aforementioned facilities are also available upon request to the Authors. The OGS bulletins, available at (Brondi et al., 2024; Snidarcig et al., 2017; Snidarcig et al., 2018; Snidarcig et al., 2019; Snidarcig et al., 2020; Snidarcig et al., 2021; Snidarcig et al., 2022), were used to guide the data download; sites include translation functionality. Information on the historical earthquakes cited in the Discussion is available at (Rovida et al., 2022); site includes translation functionality. Information on seismic station classification is available at (Luzi et al., 2020). The moment magnitude used to anchor the source spectra fit was retrieved from the Italian Seismological Instrumental and Parametric Database (ISIDe), available at (ISIDe Working Group, 2007); site includes translation functionality. The seismogenic faults cited in the Discussion are available at (DISS Working Group, 2021). All websites were last accessed in October 2024.

Acknowledgments

The authors are grateful to the Editor R. Abercrombie, to the Associate Editor and to two anonymous reviewers for thoroughly providing constructive comments and suggestions. Thanks are also due to Paolo Di Bartolomeo (OGS) and Enrico Magrin (OGS) for their technical support in the data retrieval. The RF network has recently been renamed as "Friuli Venezia Giulia and Veneto Accelerometric Network." The former ZAMG institute is currently named GeoSphere Austria. This study was carried out within the RETURN Extended Partnership and received funding from the European Union Next-GenerationEU (National Recovery and Resilience Plan - NRRP, Mission 4, Component 2, Investment 1.3 - D.D. 1243 2/8/2022, PE0000005 RETURN - CUP F83C22001660002). This research has been financially supported by the EPOS Research Infrastructure through the contribution of the Italian Ministry of University and Research (MUR). Open access publishing facilitated by Istituto Nazionale di Oceanografia e Geofisica Sperimentale, as part of the Wiley - CRUI-CARE agreement.

References

Abercrombie, R. E. (1995). Earthquake source scaling relationships from −1 to 5 M_L using seismograms recorded at 2.5-km depth. *Journal of Geophysical Research*, *100*(B12), 24015–24036. https://doi.org/10.1029/95JB02397

Abercrombie, R. E. (2021). Resolution and uncertainties in estimates of earthquake stress drop and energy release. *Philosophical Transactions of the Royal Society A*, *379*(2196), 20200131. https://doi.org/10.1098/rsta.2020.0131

Abercrombie, R. E., Baltay, A., Chu, S., Taira, T., Bindi, D., Boyd, O. S., et al. (2025). Overview of the SCEC/USGS community stress drop validation study using the 2019 ridgecrest earthquake sequence. *Bulletin of the Seismological Society of America*, *115*(3), 734–759. https://doi.org/10.1785/0120240158

Abercrombie, R. E., & Baltay, A. S. (2025). Magnitude, depth, and methodological variations of spectral stress drop within the SCEC/USGS community stress drop validation study using the 2019 ridgecrest earthquake sequence. *Bulletin of the Seismological Society of America*, *115*(6), 2741–2768. https://doi.org/10.1785/0120250056

Abercrombie, R. E., Trugman, D. T., Shearer, P. M., Chen, X., Zhang, J., Pennington, C. N., et al. (2021). Does earthquake stress drop increase with depth in the crust? *Journal of Geophysical Research: Solid Earth*, *126*(10), e2021JB022314. https://doi.org/10.1029/2021JB022314

Aki, K. (1967). Scaling law of seismic spectrum. *Journal of Geophysical Research*, *72*(4), 1217–1231. https://doi.org/10.1029/JZ072i004p01217

AlpArray Seismic Network. (2015). AlpArray Seismic Network (AASN) temporary component [Dataset]. *AlpArray Working Group*. https://doi.org/10.12686/ALPARRAY/Z3_2015

Andreson, J. G., & Hough, S. E. (1984). A model for the shape of the Fourier amplitude spectrum of acceleration at high frequencies. *Bulletin of the Seismological Society of America*, *74*, 1969–1993. https://doi.org/10.1785/BSSA0740062685

Andrews, D. J. (1986). Objective determination of source parameters and similarity of earthquakes of different size. In S. Das, J. Boatwright, & C. H. Scholz (Eds.), *Earthquake source mechanics* (pp. 259–267). American Geophysical Union. https://doi.org/10.1029/GM037p0259

Baltay, A., Abercrombie, R. E., Chu, S., & Taira, T. (2024). The SCEC/USGS community stress drop validation study using the 2019 ridgecrest earthquake sequence. *Seismica*, *3*(1). https://doi.org/10.26443/seismica.v3i1.1009

Baltay, A., Abercrombie, R. E., Oth, A., & Uchide, T. (2025). Introduction to the special section on improving measurements of earthquake source parameters. *Bulletin of the Seismological Society of America*, *115*(3), 723–733. https://doi.org/10.1785/0120250055

Baltay, A. S., Hanks, T. C., & Abrahamson, N. A. (2019). Earthquake stress drop and arias intensity. *Journal of Geophysical Research: Solid Earth*, *124*(4), 3838–3852. https://doi.org/10.1029/2018JB016753

Beeler, N. M., Wong, T.-F., & Hickman, S. H. (2003). On the expected relationships among apparent stress, static stress drop, effective shear fracture energy, and efficiency. *Bulletin of the Seismological Society of America*, *93*(3), 1381–1389. https://doi.org/10.1785/0120020162

Bindi, D., & Kotha, S. R. (2020). Spectral decomposition of the Engineering Strong Motion (ESM) flat file: Regional attenuation, source scaling and Arias stress drop. *Bulletin of Earthquake Engineering*, *18*(6), 2581–2606. https://doi.org/10.1007/s10518-020-00796-1

Bindi, D., Picozzi, M., Oth, A., & Spallarossa, D. (2025). Impact of seismic attenuation corrections on source parameter estimation. *Seismica*, *4*(2). https://doi.org/10.26443/seismica.v4i2.1651

Bindi, D., Picozzi, M., Spallarossa, D., Cotton, F., & Kotha, S. R. (2019). Impact of magnitude selection on aleatory variability associated with ground-motion prediction equations: Part II—Analysis of the between-event distribution in central Italy. *Bulletin of the Seismological Society of America*, *109*(1), 251–262. https://doi.org/10.1785/0120180239

Bindi, D., Spallarossa, D., Picozzi, M., & Morasca, P. (2020). Reliability of source parameters for small events in central Italy: Insights from spectral decomposition analysis applied to both synthetic and real data. *Bulletin of the Seismological Society of America*, *110*(6), 3139–3157. https://doi.org/10.1785/0120200126

Bindi, D., Spallarossa, D., Picozzi, M., Oth, A., Morasca, P., & Mayeda, K. (2023a). The community stress-drop validation study—Part I: Source, propagation, and site decomposition of fourier spectra. *Seismological Research Letters*. https://doi.org/10.1785/0220230019

Bindi, D., Spallarossa, D., Picozzi, M., Oth, A., Morasca, P., & Mayeda, K. (2023b). The community stress-drop validation Study—Part II: Uncertainties of the source parameters and stress drop analysis. *Seismological Research Letters*. https://doi.org/10.1785/0220230020

Bindi, D., Spallarossa, D., Picozzi, M., & Tarchini, G. (2025). Scaling and depth variability of source parameters in central and Southern Italy using regional attenuation models. *Bulletin of the Seismological Society of America*, *115*(3), 983–999. https://doi.org/10.1785/0120240144

Boatwright, J. (1980). A spectral theory for circular seismic sources: Simple estimates of source dimension, dynamic stress drop and radiated seismic energy. *Bulletin of the Seismological Society of America*, *70*, 1–27. https://doi.org/10.1785/BSSA0700010001

Boore, D. M., & Boatwright, J. (1984). Average body-wave radiation coefficients. *Bulletin of the Seismological Society of America*, *74*(5), 1615–1621. https://doi.org/10.1785/BSSA0740051615

Borok, V. K. (1959). On estimation of the displacement in an earthquake source and of source dimensions. *Annals of Geophysics*, *12*(2). https://doi.org/10.4401/ag-5718

Boyd, O. S., McNamara, D. E., Hartzell, S., & Choy, G. (2017). Influence of lithostatic stress on earthquake stress drops in North America. *Bulletin of the Seismological Society of America*, *107*(2), 856–868. https://doi.org/10.1785/0120160219

Bragato, P. L. (2021). Systematic triggering of large earthquakes by Karst Water recharge: Statistical evidence in Northeastern Italy. *Frontiers in Earth Science*, *9*, 664932. https://doi.org/10.3389/feart.2021.664932

Bragato, P. L., Comelli, P., Saraò, A., Zuliani, D., Moratto, L., Poggi, V., et al. (2021). The OGS–Northeastern Italy seismic and deformation network: Current status and outlook. *Seismological Research Letters*, *92*(3), 1704–1716. https://doi.org/10.1785/0220200372

Bressan, G., Bragato, P. L., & Venturini, C. (2003). Stress and strain tensors based on focal mechanisms in the seismotectonic framework of the Friuli-Venezia Giulia Region (Northeastern Italy). *Bulletin of the Seismological Society of America*, *93*(3), 1280–1297. https://doi.org/10.1785/0120020058

Brondi, P., Snidarcig, A., Bernardi, P., Bragato, P. L., & Di Bartolomeo, P. (2024). Bulletin of the Seismometric Network of North-Eastern Italy (RSINO), year 2022 [Dataset]. *National Institute of Oceanography and Applied Geophysics - OGS*. https://doi.org/10.13120/W1VP-B578

Brune, J. N. (1970). Tectonic stress and the spectra of seismic shear waves from earthquakes. *Journal of Geophysical Research*, *75*(26), 4997–5009. https://doi.org/10.1029/JB075i026p04997

Brune, J. N. (1971). Correction [to "Tectonic stress and the spectra, of seismic shear waves from earthquakes"]. *Journal of Geophysical Research*, *76*(20), 5002. https://doi.org/10.1029/JB076i020p05002

Calderoni, G., Rovelli, A., & Di Giovambattista, R. (2019). Stress drop, apparent stress, and radiation efficiency of clustered earthquakes in the nucleation volume of the 6 April 2009, M_w 6.1 L'Aquila earthquake. *Journal of Geophysical Research: Solid Earth*, *124*(10), 10360–10375. https://doi.org/10.1029/2019JB017513

Cantore, L., Oth, A., Parolai, S., & Bindi, D. (2011). Attenuation, source parameters and site effects in the Irpinia–Basilicata region (southern Apennines, Italy). *Journal of Seismology*, *15*(2), 375–389. https://doi.org/10.1007/s10950-011-9230-2

Castro, R. R., Andreson, J. G., & Singh, S. K. (1990). Site response, attenuation and source spectra of S waves along the Guerrero, Mexico, subduction zone. *Bulletin of the Seismological Society of America*, *80*, 1481–1503. https://doi.org/10.1785/BSSA08006A1481

Castro, R. R., Pacor, F., Sala, A., & Petrungaro, C. (1996). *S* wave attenuation and site effects in the region of Friuli, Italy. *Journal of Geophysical Research*, *101*(B10), 22355–22369. https://doi.org/10.1029/96JB02295

Cataldi, L., Picozzi, M., D'Amico, M., Morasca, P., Bindi, D., Poggi, V., et al. (2025). Supplements to "Stress drop and seismic efficiency distributions over the Adriatic indenter (European Southeastern Alps)" [Dataset]. *Zenodo*. https://doi.org/10.5281/zenodo.15052353

Cataldi, L., Poggi, V., Costa, G., Parolai, S., & Edwards, B. (2023). Parametric spectral inversion of seismic source, path and site parameters: Application to northeast Italy. *Geophysical Journal International*, *232*(3), 1926–1943. https://doi.org/10.1093/gji/ggac431

CEN. (2006). Eurocode 8: Design of structures for earthquake resistance. No. EN 1998.

Chang, H., Abercrombie, R. E., & Nakata, N. (2025). Importance of considering near-surface attenuation in earthquake source parameter estimation: Insights from Kappa at a dense array in Oklahoma. *Bulletin of the Seismological Society of America*, *115*(3), 947–964. https://doi.org/10.1785/0120240137

Chapman, M. C., & Godbee, R. W. (2012). Modeling geometrical spreading and the relative amplitudes of vertical and horizontal high-frequency ground motions in Eastern North America. *Bulletin of the Seismological Society of America*, *102*(5), 1957–1975. https://doi.org/10.1785/0120110081

Chen, X., Wu, Q., & Pennington, C. (2025). Factors that influence variability in stress-drop measurements using spectral decomposition and spectral-ratio methods for the 2019 ridgecrest earthquake sequence. *Bulletin of the Seismological Society of America*, *115*(3), 825–838. https://doi.org/10.1785/0120240150

Cipar, J. (1980). Teleseismic observations of the 1976 Friuli, Italy, earthquake sequence. *Bulletin of the Seismological Society of America*, *70*, 963–983.

Cocco, M., Tinti, E., & Cirella, A. (2016). On the scale dependence of earthquake stress drop. *Journal of Seismology*, *20*(4), 1151–1170. https://doi.org/10.1007/s10950-016-9594-4

Cochran, E. S., Baltay, A., Chu, S., Abercrombie, R. E., Bindi, D., Chen, X., et al. (2024). SCEC/USGS community stress-drop validation study: How spectral fitting approaches influence measured source parameters. *Bulletin of the Seismological Society of America*, *115*(3), 760–776. https://doi.org/10.1785/0120240140

Cultrera, G., Bordoni, P., Mercuri, A., Quintiliani, M., Minarelli, L., Famiani, D., et al. (2022). *Database for site characterization of permanent seismic stations (CRISP)*. Istituto Nazionale di Geofisica e Vulcanologia (INGV). https://doi.org/10.13127/CRISP

D'Amico, M., Morasca, P., & Spallarossa, D. (2024). GITpy, a python framework for the Generalized Inversion of Fourier Amplitude Spectra and the physical parametrization of Attenuation and Source Spectra [Software]. *Istituto Nazionale di Geofisica e Vulcanologia and Genova University*. Retrieved from https://gitlab.rm.ingv.it/inversion/gitpy/-/releases

D'Amico, M. C., Morasca, P., Spallarossa, D., Bindi, D., Picozzi, M., & Vitrano, L. (2025). User manual of GITpy: A python-based tool for the generalized inversion technique. *Rapporti Tecnici INGV*, *494*, 1–46. https://doi.org/10.13127/RPT/494

Di Bona, M. (2016). A local magnitude scale for crustal earthquakes in Italy. *Bulletin of the Seismological Society of America*, *106*(1), 242–258. https://doi.org/10.1785/0120150155

DISS Working Group. (2021). Database of Individual Seismogenic Sources (DISS), version 3.3.0: A compilation of potential sources for earthquakes larger than M 5.5 in Italy and surrounding areas [Dataset]. *Istituto Nazionale di Geofisica e Vulcanologia (INGV)*. https://doi.org/10.13127/DISS3.3.0

Drouet, S., Chevrot, S., Cotton, F., & Souriau, A. (2008). Simultaneous inversion of source spectra, attenuation parameters, and site responses: Application to the data of the French accelerometric network. *Bulletin of the Seismological Society of America*, *98*(1), 198–219. https://doi.org/10.1785/0120060215

Durand, V., Bentz, S., Kwiatek, G., Dresen, G., Wollin, C., Heidbach, O., et al. (2020). A two-scale preparation phase preceded an Mw 5.8 earthquake in the Sea of Marmara offshore Istanbul, Turkey. *Seismological Research Letters*, *91*(6), 3139–3147. https://doi.org/10.1785/0220200110

Eshelby, J. D. (1957). The determination of the elastic field of an ellipsoidal inclusion, and related problems. *Proceedings of the Royal Society of London - Series A: Mathematical and Physical Sciences*, *241*(1226), 376–396. https://doi.org/10.1098/rspa.1957.0133

Fitzko, F., Suhadolc, P., Aoudia, A., & Panza, G. F. (2005). Constraints on the location and mechanism of the 1511 Western-Slovenia earthquake from active tectonics and modeling of macroseismic data. *Tectonophysics*, *404*(1–2), 77–90. https://doi.org/10.1016/j.tecto.2005.05.003

Franceschina, G., Kravanja, S., & Bressan, G. (2006). Source parameters and scaling relationships in the Friuli-Venezia Giulia (Northeastern Italy) region. *Physics of the Earth and Planetary Interiors*, *154*(2), 148–167. https://doi.org/10.1016/j.pepi.2005.09.004

Frankel, A. (1991). Mechanisms of seismic attenuation in the crust: Scattering and anelasticity in New York state, South Africa, and southern California. *Journal of Geophysical Research*, *96*(B4), 6269–6289. https://doi.org/10.1029/91JB00192

Geological Survey-Provincia Autonoma di Trento. (1981). Trentino seismic network [Dataset]. *International Federation of Digital Seismograph Networks*. https://doi.org/10.7914/SN/ST

Goertz-Allmann, B. P., & Edwards, B. (2014). Constraints on crustal attenuation and three-dimensional spatial distribution of stress drop in Switzerland. *Geophysical Journal International*, *196*(1), 493–509. https://doi.org/10.1093/gji/ggt384

Guidoboni, E., Comastri, A., & Boschi, E. (2005). The "exceptional" earthquake of 3 January 1117 in the Verona area (northern Italy): A critical time review and detection of two lost earthquakes (lower Germany and Tuscany). *Journal of Geophysical Research*, *110*(B12), 2005JB003683. https://doi.org/10.1029/2005JB003683

Guidoboni, E., Ferrari, G., Tarabusi, G., Sgattoni, G., Comastri, A., Mariotti, D., et al. (2019). CFTI5Med, the new release of the catalogue of strong earthquakes in Italy and in the Mediterranean area. *Scientific Data*, *6*(1), 80. https://doi.org/10.1038/s41597-019-0091-9

Hough, S. E. (1996). Observational constraints on earthquake source scaling: Understanding the limits in resolution. *Tectonophysics*, *261*(1–3), 83–95. https://doi.org/10.1016/0040-1951(96)00058-3

Hunter, J. D. (2007). Matplotlib: A 2D graphics environment. *Computing in Science & Engineering*, *9*(3), 90–95. https://doi.org/10.1109/MCSE.2007.55

Ide, S., & Beroza, G. C. (2001). Does apparent stress vary with earthquake size? *Geophysical Research Letters*, *28*(17), 3349–3352. https://doi.org/10.1029/2001GL013106

ISIDe Working Group. (2007). Italian seismological instrumental and parametric database (ISIDe) [Dataset]. *Istituto Nazionale di Geofisica e Vulcanologia (INGV)*. https://doi.org/10.13127/ISIDE

Istituto Nazionale di Oceanografia e di Geofisica Sperimentale & University of Trieste. (2002). North-East Italy broadband network [Dataset]. *International Federation of Digital Seismograph Networks*. https://doi.org/10.7914/SN/NI

Istituto Nazionale di Geofisica e Vulcanologia (INGV). (2005). Rete Sismica Nazionale (RSN) [Dataset]. *Istituto Nazionale di Geofisica e Vulcanologia (INGV)*. https://doi.org/10.13127/SD/X0FXNH7QFY

Istituto Nazionale di Oceanografia e di Geofisica Sperimentale - OGS. (2016). North-East Italy seismic network [Dataset]. *International Federation of Digital Seismograph Networks*. https://doi.org/10.7914/SN/OX

Kanamori, H., & Rivera, L. (2004). Static and dynamic scaling relations for earthquakes and their implications for rupture speed and stress drop. *Bulletin of the Seismological Society of America*, *94*(1), 314–319. https://doi.org/10.1785/0120030159

Kanamori, H., Hauksson, E., Hutton, L. K., & Jones, L. M. (1993). Determination of earthquake energy release and ML using TERRAscope. *Bulletin of the Seismological Society of America*, *83*, 330–346. https://doi.org/10.1785/BSSA0830020330

Kemna, K. B., Verdecchia, A., & Harrington, R. M. (2021). Spatio-temporal evolution of earthquake static stress drop values in the 2016–2017 central Italy seismic sequence. *Journal of Geophysical Research: Solid Earth*, *126*(11), e2021JB022566. https://doi.org/10.1029/2021JB022566

Klin, P., Laurenzano, G., Barnaba, C., Priolo, E., & Parolai, S. (2021). Site amplification at permanent stations in northeastern Italy. *Bulletin of the Seismological Society of America*, *111*(4), 1885–1904. https://doi.org/10.1785/0120200361

Klin, P., Laurenzano, G., & Priolo, E. (2018). GITANES: A MATLAB package for estimation of site spectral amplification with the generalized inversion technique. *Seismological Research Letters*, *89*(1), 182–190. https://doi.org/10.1785/0220170080

Konno, K., & Ohmachi, T. (1998). Ground-motion characteristics estimated from spectral ratio between horizontal and vertical components of microtremor. *Bulletin of the Seismological Society of America*, *88*(1), 228–241. https://doi.org/10.1785/BSSA0880010228

Lockner, D. A., & Okubo, P. G. (1983). Measurements of frictional heating in granite. *Journal of Geophysical Research*, *88*(B5), 4313–4320. https://doi.org/10.1029/JB088iB05p04313

Lomax, A., Virieux, J., Volant, P., & Berge-Thierry, C. (2000). Probabilistic earthquake location in 3D and layered models. In C. H. Thurber & N. Rabinowitz (Eds.), *Advances in seismic event location. Modern approaches in geophysics* (Vol. 18, pp. 101–134). Springer. https://doi.org/10.1007/978-94-015-9536-0_5

Luzi, L., Lanzano, G., Felicetta, C., D'Amico, M. C., Russo, E., Sgobba, S., et al. (2020). Engineering Strong Motion Database (ESM) (version 2.0) [Dataset]. *Istituto Nazionale di Geofisica e Vulcanologia (INGV)*. https://doi.org/10.13127/ESM.2

Madariaga, R. (1976). Dynamics of an expanding circular fault. *Bulletin of the Seismological Society of America*, *66*(3), 639–666. https://doi.org/10.1785/BSSA0660030639

Madariaga, R. (1979). On the relation between seismic moment and stress drop in the presence of stress and strength heterogeneity. *Journal of Geophysical Research*, *84*(B5), 2243–2250. https://doi.org/10.1029/JB084iB05p02243

Magrin, A., & Rossi, G. (2020). Deriving a new crustal model of northern Adria: The Northern Adria Crust (NAC) model. *Frontiers in Earth Science*, *8*, 89. https://doi.org/10.3389/feart.2020.00089

Malagnini, L., Akinci, A., Hermann, R., Pino, N., & Scognamiglio, L. (2002). Characteristics of the ground motion in Northeastern Italy. *Bulletin of the Seismological Society of America*, *92*(6), 2186–2204. https://doi.org/10.1785/0120010219

Malagnini, L., Scognamiglio, L., Mercuri, A., Akinci, A., & Mayeda, K. (2008). Strong evidence for non-similar earthquake source scaling in central Italy. *Geophysical Research Letters*, *35*(17), 2008GL034310. https://doi.org/10.1029/2008GL034310

Massa, M., Rizzo, A. L., Lorenzetti, A., Lovati, S., D'Alema, E., Puglia, R., et al. (2021). Rete di monitoraggio multiparametrico del Garda (Nord Italia)—PDnet (Version 1.0) [Dataset]. *Istituto Nazionale di Geofisica e Vulcanologia (INGV)*. https://doi.org/10.13127/SD/YHCFOMCBO_

Massironi, M., Zampieri, D., & Caporali, A. (2006). Miocene to present major fault linkages through the Adriatic indenter and the Austroalpine—Penninic collisional wedge (Alps of NE Italy). *Geological Society, London, Special Publications*, *262*(1), 245–258. https://doi.org/10.1144/GSL.SP.2006.262.01.15

Mayeda, K., Hofstetter, A., O'Boyle, J. L., & Walter, W. R. (2003). Stable and transportable regional magnitudes based on coda-derived moment-rate spectra. *Bulletin of the Seismological Society of America*, *93*(1), 224–239. https://doi.org/10.1785/0120020020

Mayeda, K., & Walter, W. R. (1996). Moment, energy, stress drop, and source spectra of western United States earthquakes from regional coda envelopes. *Journal of Geophysical Research*, *101*(B5), 11195–11208. https://doi.org/10.1029/96JB00112

MedNet Project Partner Institutions. (1990). Mediterranean very broadband seismographic network (MedNet) [Dataset]. *Istituto Nazionale di Geofisica e Vulcanologia (INGV)*. https://doi.org/10.13127/SD/FBBBTDTD6Q

Morasca, P., Bindi, D., Mayeda, K., Roman-Nieves, J., Barno, J., Walter, W. R., & Spallarossa, D. (2022). Source scaling comparison and validation in Central Italy: Data intensive direct *S* waves versus the sparse data coda envelope methodology. *Geophysical Journal International*, *231*(3), 1573–1590. https://doi.org/10.1093/gji/ggac268

Morasca, P., Walter, W., Mayeda, K., & Massa, M. (2019). Evaluation of earthquake stress parameters and its scaling during the 2016-2017 Amatrice-Norcia-Visso sequence—Part I. *Geophysical Journal International*, *218*(1), 446–455. https://doi.org/10.1093/gji/ggz165

Mori, J., & Frankel, A. (1990). Source parameters from small events associated with the 1986 North Palm Springs, California, earthquake, determined using empirical Green functions. *Bulletin of the Seismological Society of America*, *80*, 278–295. https://doi.org/10.1785/BSSA0800020278

Neely, J. S., Park, S., & Baltay, A. (2025). The impact of source time function complexity on stress-drop estimates. *Bulletin of the Seismological Society of America*, *115*(3), 1149–1161. https://doi.org/10.1785/0120240022

Oth, A., Bindi, D., Parolai, S., & Di Giacomo, D. (2011). Spectral analysis of K-NET and KiK-net data in Japan, part II: On attenuation characteristics, source spectra, and site response of borehole and surface stations. *Bulletin of the Seismological Society of America*, *101*(2), 667–687. https://doi.org/10.1785/0120100135

Oth, A., & Kaiser, A. E. (2014). Stress release and source scaling of the 2010–2011 Canterbury, New Zealand earthquake sequence from spectral inversion of ground motion data. *Pure and Applied Geophysics*, *171*(10), 2767–2782. https://doi.org/10.1007/s00024-013-0751-1

Oth, A., Miyake, H., & Bindi, D. (2017). On the relation of earthquake stress drop and ground motion variability. *Journal of Geophysical Research: Solid Earth*, *122*(7), 5474–5492. https://doi.org/10.1002/2017JB014026

Pacor, F., Spallarossa, D., Oth, A., Luzi, L., Puglia, R., Cantore, L., et al. (2016). Spectral models for ground motion prediction in the L'Aquila region (central Italy): Evidence for stress-drop dependence on magnitude and depth. *Geophysical Journal International*, *204*(2), 697–718. https://doi.org/10.1093/gji/ggv448

Paige, C. C., & Saunders, M. A. (1982). LSQR: An algorithm for sparse linear equations and sparse least squares. *ACM Transactions on Mathematical Software*, *8*(1), 43–71. https://doi.org/10.1145/355984.355989

Parolai, S., Bindi, D., Baumbach, M., Grosser, H., Milkereit, C., Karakisa, S., & Zünbül, S. (2004). Comparison of different site response estimation techniques using aftershocks of the 1999 Izmit earthquake. *Bulletin of the Seismological Society of America*, *94*(3), 1096–1108. https://doi.org/10.1785/0120030086

Pérez-Campos, X., & Beroza, G. C. (2001). An apparent mechanism dependence of radiated seismic energy. *Journal of Geophysical Research*, *106*(B6), 11127–11136. https://doi.org/10.1029/2000JB900455

Picozzi, M., Bindi, D., Festa, G., Cotton, F., Scala, A., & D'Agostino, N. (2021). Spatiotemporal evolution of microseismicity seismic source properties at the Irpinia near-fault observatory, Southern Italy. *Bulletin of the Seismological Society of America*, *112*(1), 226–242. https://doi.org/10.1785/0120210064

Picozzi, M., Bindi, D., Zollo, A., Festa, G., & Spallarossa, D. (2019). Detecting long-lasting transients of earthquake activity on a fault system by monitoring apparent stress, ground motion and clustering. *Scientific Reports*, *9*(1), 16268. https://doi.org/10.1038/s41598-019-52756-8

Picozzi, M., Iaccarino, A. G., Spallarossa, D., & Bindi, D. (2023). On catching the preparatory phase of damaging earthquakes: An example from central Italy. *Scientific Reports*, *13*(1), 14403. https://doi.org/10.1038/s41598-023-41625-0

Picozzi, M., Oth, A., Parolai, S., Bindi, D., De Landro, G., & Amoroso, O. (2017). Accurate estimation of seismic source parameters of induced seismicity by a combined approach of generalized inversion and genetic algorithm: Application to the Geysers geothermal area, California. *Journal of Geophysical Research: Solid Earth*, *122*(5), 3916–3933. https://doi.org/10.1002/2016JB013690

Picozzi, M., Spallarossa, D., Bindi, D., Iaccarino, A. G., & Rivalta, E. (2022). Detection of spatial and temporal stress changes during the 2016 central Italy seismic sequence by monitoring the evolution of the energy index. *Journal of Geophysical Research: Solid Earth*, *127*(11), e2022JB025100. https://doi.org/10.1029/2022JB025100

Pondrelli, S., Salimbeni, S., Ekström, G., Morelli, A., Gasperini, P., & Vannucci, G. (2006). The Italian CMT dataset from 1977 to the present. *Physics of the Earth and Planetary Interiors*, *159*(3–4), 286–303. https://doi.org/10.1016/j.pepi.2006.07.008

Presidency of Counsil of Ministers - Civil Protection Department. (1972). Italian strong motion network [Dataset]. *International Federation of Digital Seismograph Networks*. https://doi.org/10.7914/SN/IT

Reiter, F., Freudenthaler, C., Hausmann, H., Ortner, H., Lenhardt, W., & Brandner, R. (2018). Active seismotectonic deformation in front of the dolomites indenter, eastern alps. *Tectonics*, *37*(12), 4625–4654. https://doi.org/10.1029/2017TC004867

Restivo, A., Barnaba, C., & Michelini, A. (2006). Site effects study in the Serravalle village (NE Italy) by means of spectral ratios analyses relatively to multiple reference sites. *Natural Hazards*, *39*(1), 31–49. https://doi.org/10.1007/s11069-005-2960-0

Riggio, A., & Russi, M. (1984). Procedura di analisi ed elaborazione dei dati registrati da reti sismometriche locali. In *Finalità Ed Esperienze Della Rete Sismometrica Del Friuli-Venezia Giulia* (pp. 53–74). Testo Delle Comunicazioni.

Rovida, A., Locati, M., Camassi, R., Lolli, B., & Gasperini, P. (2020). The Italian earthquake catalogue CPTI15. *Bulletin of Earthquake Engineering*, *18*(7), 2953–2984. https://doi.org/10.1007/s10518-020-00818-y

Rovida, A., Locati, M., Camassi, R., Lolli, B., Gasperini, P., & Antonucci, A. (2022). Italian Parametric Earthquake Catalogue (CPTI15), version 4.0 [Dataset]. *Istituto Nazionale di Geofisica e Vulcanologia (INGV)*. https://doi.org/10.13127/CPTI/CPTI15.4

Sandron, D., Rebez, A., Tamaro, A., & Slejko, D. (2023). Recent earthquakes (2000-2021) in and around the Friuli Venezia Giulia region (NE Italy) and quality improvements of the OGS network monitoring capabilities. *Bulletin of the Geophysical Observatory*, *64*(3), 237–258. https://doi.org/10.4430/bgo00421

Savage, J. C., & Wood, M. D. (1971). The relation between apparent stress and stress drop. *Bulletin of the Seismological Society of America*, *61*, 1381–1388. https://doi.org/10.1785/BSSA0610051381

Scafidi, D., Spallarossa, D., Ferretti, G., Barani, S., Castello, B., & Margheriti, L. (2019). A complete automatic procedure to compile reliable seismic catalogs and travel-time and strong-motion parameters datasets. *Seismological Research Letters*, *90*(3), 1308–1317. https://doi.org/10.1785/0220180257

Serpelloni, E., Vannucci, G., Anderlini, L., & Bennett, R. A. (2016). Kinematics, seismotectonics and seismic potential of the eastern sector of the European Alps from GPS and seismic deformation data. *Tectonophysics*, *688*, 157–181. https://doi.org/10.1016/j.tecto.2016.09.026

Shearer, P. M., Abercrombie, R. E., Trugman, D. T., & Wang, W. (2019). Comparing EGF methods for estimating corner frequency and stress drop from *P* wave spectra. *Journal of Geophysical Research: Solid Earth*, *124*(4), 3966–3986. https://doi.org/10.1029/2018JB016957

Shearer, P. M., Prieto, G. A., & Hauksson, E. (2006). Comprehensive analysis of earthquake source spectra in southern California. *Journal of Geophysical Research*, *111*(B6), 2005JB003979. https://doi.org/10.1029/2005JB003979

Shearer, P. M., Vandevert, I., Fan, W., Abercrombie, R. E., Bindi, D., Calderoni, G., et al. (2024). Earthquake source spectra estimates vary widely for two ridgecrest aftershocks because of differences in attenuation corrections. *Bulletin of the Seismological Society of America*, *115*(3), 777–791. https://doi.org/10.1785/0120240134

Shelly, D. R., Mayeda, K., Barno, J., Whidden, K. M., Moschetti, M. P., Llenos, A. L., et al. (2021). A big problem for small earthquakes: Benchmarking routine magnitudes and conversion relationships with coda envelope-derived Mw in Southern Kansas and Northern Oklahoma. *Bulletin of the Seismological Society of America*, *112*(1), 210–225. https://doi.org/10.1785/0120210115

Slejko, D., Neri, G., Orozova, I., Renner, G., & Wyss, M. (1999). Stress field in Friuli (NE Italy) from fault plane solutions of activity following the 1976 main shock. *Bulletin of the Seismological Society of America*, *89*(4), 1037–1052. https://doi.org/10.1785/BSSA0890041037

Slovenian Environment Agency. (1990). Seismic network of the Republic of Slovenia [Dataset]. *International Federation of Digital Seismograph Networks*. https://doi.org/10.7914/SN/SL

Snidarcig, A., Bernardi, P., Bragato, P. L., Di Bartolomeo, P., Garbin, M., & Urban, S. (2017). Bulletin of the Seismometric Network of North-Eastern Italy (RSINO), Year 2016 [Dataset]. *Istituto Nazionale di Oceanografia e di Geofisica Sperimentale - OGS*. https://doi.org/10.6092/A608D853-755E-4177-AADA-992857CCB44E

Snidarcig, A., Bernardi, P., Bragato, P. L., Di Bartolomeo, P., Garbin, M., & Urban, S. (2018). Bulletin of the Seismometric Network of North-Eastern Italy (RSINO), Year 2017 [Dataset]. *Istituto Nazionale di Oceanografia e di Geofisica Sperimentale - OGS*. https://doi.org/10.6092/3FF3C323-D7A4-4183-BEA0-1A53814AC8B9

Snidarcig, A., Bernardi, P., Bragato, P. L., Di Bartolomeo, P., Garbin, M., & Urban, S. (2019). Bulletin of the Seismometric Network of North-Eastern Italy (RSINO), Year 2018 [Dataset]. *Istituto Nazionale di Oceanografia e di Geofisica Sperimentale - OGS*. https://doi.org/10.6092/C53F37CE-BCF3-453C-A2CF-1894D48CFBBB

Snidarcig, A., Bernardi, P., Bragato, P. L., Di Bartolomeo, P., Garbin, M., & Urban, S. (2020). Bulletin of the Seismometric Network of North-Eastern Italy (RSINO), Year 2019 [Dataset]. *Istituto Nazionale di Oceanografia e di Geofisica Sperimentale - OGS*. https://doi.org/10.6092/58FF169A-2F02-46AE-908A-BDFCACEA069C

Snidarcig, A., Bernardi, P., Bragato, P. L., Di Bartolomeo, P., Garbin, M., & Urban, S. (2021). Bulletin of the seismometric network of North-Eastern Italy (RSINO), year [Dataset]. *Istituto Nazionale di Oceanografia e di Geofisica Sperimentale - OGS*. https://doi.org/10.13120/108B8D94-361A-45F3-8195-FC4E8F73D264

Snidarcig, A., Bernardi, P., Bragato, P. L., Di Bartolomeo, P., Garbin, M., & Urban, S. (2022). Bulletin of the Seismometric Network of North-Eastern Italy (RSINO), Year 2021 [Dataset]. *Istituto Nazionale di Oceanografia e di Geofisica Sperimentale - OGS*. https://doi.org/10.13120/8B252B09-314F-456F-812A-B05268ECD001

Spallarossa, D., Picozzi, M., Scafidi, D., Morasca, P., Turino, C., & Bindi, D. (2021). The RAMONES service for rapid assessment of seismic moment and radiated energy in central Italy: Concepts, capabilities, and future perspectives. *Seismological Research Letters*, *92*(3), 1759–1772. https://doi.org/10.1785/0220200348

Strollo, A., Cambaz, D., Clinton, J., Danecek, P., Evangelidis, C. P., Marmureanu, A., et al. (2021). EIDA: The European integrated data archive and service infrastructure within ORFEUS. *Seismological Research Letters*, *92*(3), 1788–1795. https://doi.org/10.1785/0220200413

Swiss Seismological Service (SED) At ETH Zurich. (1983). National seismic networks of Switzerland [Dataset]. *ETH Zürich*. https://doi.org/10.12686/SED/NETWORKS/CH

Tarchini, G., Scafidi, D., Parolai, S., Picozzi, M., Bindi, D., & Spallarossa, D. (2024). The seismic station and site amplification service: Continuously updated information on Italian seismic stations. *Seismological Research Letters*, *96*(3), 2027–2038. https://doi.org/10.1785/0220240291

The Matplotlib Development Team. (2024). Matplotlib: Visualization with Python (version v3.8.4) [Software]. *Zenodo*. https://doi.org/10.5281/ZENODO.10916799

Trugman, D. T., & Shearer, P. M. (2017). Application of an improved spectral decomposition method to examine earthquake source scaling in Southern California. *Journal of Geophysical Research: Solid Earth*, *122*(4), 2890–2910. https://doi.org/10.1002/2017JB013971

University of Trieste. (1993). Friuli Venezia giulia accelerometric network [Dataset]. *International Federation of Digital Seismograph Networks*. https://doi.org/10.7914/SN/RF

Viganò, A., Bressan, G., Ranalli, G., & Martin, S. (2008). Focal mechanism inversion in the Giudicarie–Lessini seismotectonic region (Southern Alps, Italy): Insights on tectonic stress and strain. *Tectonophysics*, *460*(1–4), 106–115. https://doi.org/10.1016/j.tecto.2008.07.008

Viganò, A., Scafidi, D., Ranalli, G., Martin, S., Della Vedova, B., & Spallarossa, D. (2015). Earthquake relocations, crustal rheology, and active deformation in the central–eastern Alps (N Italy). *Tectonophysics*, *661*, 81–98. https://doi.org/10.1016/j.tecto.2015.08.017

Viganò, A., Zampieri, D., Rossato, S., Martin, S., Selli, L., Prosser, G., et al. (2018). Past to present deformation of the central-eastern Southern Alps: From the foreland to the Giudicarie belt. *Geological Field Trips*, *10*(1.1), 1–78. https://doi.org/10.3301/GFT.2018.01

Villani, F., Antonioli, A., Pastori, M., Baccheschi, P., & Ciaccio, M. G. (2024). Stress patterns and crustal anisotropy in the Eastern alps: Insights from seismological and geological observations. *Tectonics*, *43*(3), e2023TC008033. https://doi.org/10.1029/2023TC008033

Wang, H., Ren, Y., Wen, R., & Xu, P. (2019). Breakdown of earthquake self-similar scaling and source rupture directivity in the 2016–2017 central Italy seismic sequence. *Journal of Geophysical Research: Solid Earth*, *124*(4), 3898–3917. https://doi.org/10.1029/2018JB016543

Yenier, E., & Atkinson, G. M. (2015). Regionally adjustable generic ground-motion prediction equation based on equivalent point-source simulations: Application to central and Eastern North America. *Bulletin of the Seismological Society of America*, *105*(4), 1989–2009. https://doi.org/10.1785/0120140332

ZAMG - Zentralanstalt für Meterologie und Geodynamik. (2006). Province Südtirol [Dataset]. *International Federation of Digital Seismograph Networks*. Retrieved from https://www.fdsn.org/networks/detail/SI/

ZAMG - Zentralanstalt für Meterologie und Geodynamik. (1987). Austrian seismic network [Dataset]. *International Federation of Digital Seismograph Networks*. https://doi.org/10.7914/SN/OE

Zhang, J., Chen, X., & Abercrombie, R. E. (2022). Spatiotemporal variability of earthquake source parameters at Parkfield, California, and their relationship with the 2004 M6 earthquake. *Journal of Geophysical Research: Solid Earth*, *127*(6), e2021JB022851. https://doi.org/10.1029/2021JB022851

Zollo, A., Orefice, A., & Convertito, V. (2014). Source parameter scaling and radiation efficiency of microearthquakes along the Irpinia fault zone in southern Apennines, Italy. *Journal of Geophysical Research: Solid Earth*, *119*(4), 3256–3275. https://doi.org/10.1002/2013JB010116

References From the Supporting Information

Abercrombie, R. E. (2013). Comparison of direct and coda wave stress drop measurements for the Wells, Nevada, earthquake sequence. *Journal of Geophysical Research: Solid Earth*, *118*(4), 1458–1470. https://doi.org/10.1029/2012JB009638

Oth, A., Bindi, D., Parolai, S., & Di Giacomo, D. (2010). Earthquake scaling characteristics and the scale-(in)dependence of seismic energy-to-moment ratio: Insights from KiK-net data in Japan. *Geophysical Research Letters*, *37*(19), 2010GL044572. https://doi.org/10.1029/2010GL044572